

# Realistic uncertainties on Hapke model parameters from photometric measurement

Schmidt Frédéric<sup>1,2</sup>, Fernando Jennifer<sup>1,2</sup>

<sup>1</sup> *Univ. Paris-Sud, Laboratoire GEOPS, UMR8148, Orsay, F-91405;*  
(frederic.schmidt@u-psud.fr) <sup>2</sup> *CNRS, Orsay, F-91405, France*

---

## Abstract

The single particle phase function describes the manner in which an average element of a granular material diffuses the light in the angular space usually with two parameters: the asymmetry parameter  $b$  describing the width of the scattering lobe and the backscattering fraction  $c$  describing the main direction of the scattering lobe. Hapke proposed a convenient and widely used analytical model to describe the spectro-photometry of granular materials. Using a compilation of the published data, Hapke (2012, Icarus, 221, 1079-1083) recently studied the relationship of  $b$  and  $c$  for natural examples and proposed the hockey stick relation (excluding  $b > 0.5$  and  $c > 0.5$ ). For the moment, there is no theoretical explanation for this relationship. One goal of this article is to study a possible bias due to the retrieval method.

We expand here an innovative Bayesian inversion method in order to study into detail the uncertainties of retrieved parameters. On Emission Phase Function (EPF) data, we demonstrate that the uncertainties of the retrieved parameters follow the same hockey stick relation, suggesting that this relation is due to the fact that  $b$  and  $c$  are coupled parameters in the Hapke model instead of a natural phenomena. Nevertheless, the data used in the Hapke (2012) compilation generally are full Bidirectional Reflectance Diffusion Function (BRDF) that are shown not to be subject to this artifact.

Moreover, the Bayesian method is a good tool to test if the sampling geometry is sufficient to constrain the parameters (single scattering albedo, surface roughness,  $b$ ,  $c$ , opposition effect). We performed sensitivity tests by mimicking various surface scattering properties and various single image-like/disk resolved image, EPF-like and BRDF-like geometric sampling conditions. The second goal of this article is to estimate the favorable geometric conditions for an accurate estimation of photometric parameters in order to provide new constraints for future observation campaigns and instrumentations.

**Keywords:** spectro-photometry, Hapke model, Bayesian inversion, disk resolved image, EPF, BRDF, uncertainties

---

## 1. Introduction

Photometry is the study of the surface by the angular response of the reflected light by a medium described by the Bi-directional Reflectance Distribution Function (BRDF) (Hapke, 1993).

Hapke proposed a set of approximated analytical equations to estimate conveniently the BRDF of a granular medium (e.g. Hapke, 1981; Hapke and Wells, 1981; Hapke, 1984, 1986, 2002, 2008). This formulation has been controversial for two decades (e.g. Mishchenko, 1994; Hapke, 1996; Shepard and Helfenstein, 2007; Shkuratov et al., 2012; Hapke, 2013) but due to its relative simplicity and fast computation, many authors have been using it to analyze laboratory data (e.g. Cord et al., 2003; Souchon et al., 2011; Beck et al., 2012; Pommerol et al., 2013; Johnson et al., 2013), telescopic observation (e.g. Hapke et al., 1998), in situ data (e.g. Johnson et al., 1999, 2006b,a), remote sensing data (e.g. Jehl et al., 2008; Yokota et al., 2011; Fernando et al., 2013; Vincendon, 2013; Sato et al., 2014).

The scope of this article is to discuss the properties of the Hapke model in term of data analysis, but not to discuss particular aspects of the realism of the photometric Hapke model. Some authors addressed the difficulties to fit the model to actual data, indicating that the problem is ill posed, due to parameter coupling (Mustard and Pieters, 1989; Helfenstein and Veverka, 1989; Baratoux et al., 2006; Souchon et al., 2011). The most usual ways to fit are a minimization of the  $\chi^2$ , stepwise in a grid (Shepard and Helfenstein, 2007), using the Levenberg-Marquardt method (Sato et al., 2014; Johnson et al., 2013), a simplex algorithm (Gunderson et al., 2006), and a genetic algorithm (Cord et al., 2003) and Particle Swarm Optimization (Beck et al., 2012; Pommerol et al., 2013). These strategies are relevant in the case of an unique solution (only one minimum in the  $\chi^2$ ) and close to gaussian shape around the solution. Due to the non-linearities of the Hapke equations, those two mathematical properties may not be fulfilled.

We propose here a new kind of technique, based on the Bayesian formulation to estimate the model parameters in agreement with the data (Tarantola and Valette, 1982). The general framework of Bayesian theory enabled us to: (i) take into account precisely the uncertainties of measured quantities, (ii) define precisely the range of possibility of all model parameters, (iii) estimate the range of solution in a general case (that may not have a gaussian shape). From theoretical point of view, each information is described as a probability density function (PDF): the measured quantities, the a priori parameters and the posterior parameters. Within this framework, the solution is expressed as a “final state of information” which always exists, solving the apparent ill-posed problem.

We already used this strategy to analyze the spectro-photometric data from the Compact Reconnaissance Imaging Spectrometer for Mars (CRISM) instrument (Murchie et al., 2007), after the MARS-ReCO atmospherical correction (Ceamanos et al., 2013), by estimating the PDF of all Hapke parameters of the Martian surface (Fernando et al., 2013). We also applied it on full CRISM

images on the MER landing sites (Fernando et al., 2015).

In this article, we propose to perform extensive sensitivity tests on synthetic dataset, using the Bayesian inversion, in order to study the behavior of Hapke model to fit the data. This study aims at:

1. estimating precise uncertainties level on the model parameters on different typical observation types (one image-like observation/disk resolved image, CRISM-like Emission Phase Function (EPF), very favorable EPF, Bidirectional Reflectance Distribution Function (BRDF) measurements)
2. determining the uncertainties dependance on BRDF sampling
3. evaluating the possibility to have more than one “solution”, i.e. multiple minima
4. chasing any effect which could bias the estimation of the parameters  $b$  and  $c$  leading to a fake hockey stick relationship

This work should help to interpret previous analyses but also to design future instrumental and observational campaigns.

## 2. Method

### 2.1. Direct model: the Hapke’s photometric model

Standard 1993 Hapke modeling (Hapke, 1993) is widely used in the planetary science community due to the simplicity of its expression, fast computation, and the purported physical meaning of the model parameters allowing the characterization of planetary surface materials (e.g., grain size, morphology, internal structure and surface roughness).

More recent developments are available. First, the version from Hapke, 2002 includes: (i) a more accurate analytic approximation for isotropic scatterers, (ii) a better estimation of the bidirectional reflectance when the scatterers are anisotropic, and (iii) the incorporation of coherent backscattering. Second, the version from Hapke, 2008 treats the porosity.

Following previous studies (Johnson et al., 2006b,a; Jehl et al., 2008; Beck et al., 2012; Fernando et al., 2013), we decided to use the following standard expression of Hapke’s 1993 in order to be coherent with older analysis. In addition, more recent developments are not fully validated with experimental data. We remind here the main expression:

$$r(\theta_0, \theta, g) = \frac{\omega}{4\pi} \frac{\mu_{0e}}{(\mu_{0e} + \mu_e)} \{ [1 + B(g)] P(g) + H(\mu_{0e})H(\mu_e) - 1 \} S(\theta_0, \theta, g) \quad (1)$$

Using the following quantities:

- $\theta_0$ ,  $\theta$ , and  $g$ : incidence, emergence and phase angles. The whole geometry quantities are noted  $\Omega = (\theta_0, \theta, g)$ . Terms  $\mu_{0e}$  and  $\mu_e$  are the cosine of the equivalent incidence and emergence angles, in the case of a rough surface, as defined in (Hapke, 1993). We note  $\phi$  as the azimuth angle.

- $\omega$  ( $0 \leq \omega \leq 1$ ): single scattering albedo. It represents the fraction of scattered to incident radiation by a single particle (also noted  $w$ ).
- $P(g)$ : particle scattering phase function. It characterizes the angular distribution of energy for an average particle. We used the empirical 2-term Henyey-Greenstein function (Henyey and Greenstein, 1941) (hereafter referred to as HG2) for studying planetary surfaces (Cord et al., 2003; Jehl et al., 2008; Johnson et al., 2006b,a; Souchon et al., 2011; Beck et al., 2012; Pommerol et al., 2013):

$$P(g) = (1 - c) \frac{1 - b^2}{(1 + 2b \cos(g) + b^2)^{3/2}} + c \frac{1 - b^2}{(1 - 2b \cos(g) + b^2)^{3/2}} \quad (2)$$

The HG2 function depends on two parameters: the asymmetry parameter  $b$  ( $0 \leq b \leq 1$ ) which characterizes the anisotropy of the scattering lobe (from  $b = 0$ , which corresponds to the isotropic case, to  $b = 1$ , which corresponds to a particle which diffuses light in a single direction) and the backscattering fraction  $c$  ( $0 \leq c \leq 1$ ) which characterizes the main direction of the diffusion ( $c < 0.5$  corresponding to forward scattering and  $c > 0.5$  corresponding to backward scattering).

- $H(x)$ : multiple scattering function. An analytical function for isotropic scatterers has been proposed (Hapke, 1993) with a relative error to the exact values (Chandrasekhar, 1960) lower than 1%, leading to a relative error on the BRDF lower than 2% (Cheng and Domingue, 2000). Defining  $y = (1 - \omega)^{1/2}$ , the multiple scattering function is:

$$H(x) = \left\{ 1 - [1 - y] x \left[ \left( \frac{1 - y}{1 + y} \right) + \left( 1 - \frac{1}{2} \left( \frac{1 - y}{1 + y} \right) - x \left( \frac{1 - y}{1 + y} \right) \right) \ln \left( \frac{1 + x}{x} \right) \right] \right\}^{-1} \quad (3)$$

A new expression dedicated to anisotropic scattering has been proposed (Hapke, 2002). Nevertheless, Pommerol et al. (2013) have noticed that the use of the recent  $H$  expression leads to no significant changes over the previous expression.

- $B(g)$ : opposition effect function. It describes the sharp increase of brightness around the zero phase angle often observed in the case of particulate media. Only the Shadow Hiding Opposition Effect (SHOE) is taken into account as follows (Hapke, 1993):

$$B(g) = \frac{B_0}{1 + \frac{1}{h} \tan \left( \frac{g}{2} \right)} \quad (4)$$

The function depends on the parameters  $h$  and  $B_0$  (ranging from 0 to 1) which are the angular width and the amplitude of the opposition effect respectively. The Coherent Backscattering Opposition Effect (CBOE) is ignored in our case since the minimum phase angle is large ( $g > 10^\circ$ ).

- $S(\theta_0, \theta, g)$ : macroscopic roughness factor. It describes the surface topography as a set of facets with a Gaussian distribution of tangent of the slopes, with mean slope angle noted  $\bar{\theta}$  also called surface macroscopic roughness (Hapke, 1993). This model of the surface roughness effect includes the partially shadowed area depending on the geometry and the bias on the effective incidence and emergence angles. The expression of  $S$  is given in Hapke (1993).

## 2.2. Bayesian inversion

Because the Hapke model is a non linear model and may not have a unique solution, one may use the Bayesian inversion framework based on the concept of the state of information which is characterized by a Probability Density Function (PDF) (Tarantola and Valette, 1982). This approach has already been proposed for the Hapke model (Fernando et al., 2013). To infer the solution, this approach takes into account the initial state of information (*a priori* knowledge) on the parameters and the observations and applies the Bayes' theorem to estimate the final state of information, called *a posteriori*. The key points of the concept and framework assumptions are presented in the following:

- Direct model and related quantities:
  - The direct model  $F$  estimates the simulated data  $d$ , from model parameters  $m$ :
 
$$d = F(m) \quad (5)$$
  - The parameters  $m$  include  $\omega, b, c, \bar{\theta}, B_0$  and  $h$ . The parameters  $m$  are in the parameter vector space  $M = [0, 1]^5 [0, 45]$ , since all parameters are between 0 and 1, except  $\bar{\theta}$  between 0 and  $45^\circ$ .
  - The simulated data  $d$  is the collection  $r_i = r(\Omega_i)$  for all  $i$ th peculiar geometry noted as  $\Omega_i = (\theta_0, \theta, g)_i$ . The total number of geometries is noted  $N_g$ . The simulated data  $d$  are in the observation vector space  $D = \mathbb{R}^{N_g}$ , since the BRDF is a positive quantity.
  - The model  $F(m)$  is the Hapke equation 1. We consider that the geometries have very low uncertainties, which is the case for most data in planetary science cases. Thus, the parameters  $\Omega_i$  are not estimated by the inversion.
- Observation and other *a priori* information:
  - The actual observation is considered as prior information on data  $\rho_D(d)$  in the observation space  $D$ . It is assumed to be a  $N_g$ -dimension gaussian PDF  $\mathcal{G}(o, C)$ , with mean  $o$  and covariance matrix  $C$ . The values  $o_i$  are the observation for each geometry. The covariance matrix  $C$  is assumed here to be diagonal since each measurements at a given geometry is independent of the other geometric measurements. The diagonal elements  $C_{ii}$  are  $\sigma_1^2, \dots, \sigma_{N_g}^2$ , with  $\sigma_i$  being the standard deviation.

- The prior information on model parameters  $\rho_M(m)$  in the parameter space  $M$  is independent to the data and corresponds to the state of null information if no information is available on the parameters. We consider an uniform PDF in their definition space  $M$ . Outside  $M$ , the PDF is null, avoiding unphysical solutions to appear.
- The state of null information  $\mu_D(d)$ , representing the case when no information is available, is trivial in our case and represents the uniform PDF in the parameters space  $M$ .
- Solution of inverse problems and *a posteriori* information:
  - The posterior PDF in the model space  $\sigma_M(m)$  as defined by Tarantola and Valette (1982) is:

$$\sigma_M(m) = k \rho_M(m) L(m) \quad (6)$$

where  $k$  is a constant and  $L(m)$  is the likelihood function

$$L(m) = \int_D dd \frac{\rho_D(d) \theta(d | m)}{\mu_D(d)} \quad (7)$$

where  $\theta(d | m)$  is the theoretical relationship of the PDF for  $d$  given  $m$ . We do not consider errors on the model itself, so  $\theta(d | m) = \delta(F(m))$ .

- The solution of the general inverse problem is given by the PDF  $\sigma_M(m)$ . The best way to represent  $\sigma_M(m)$  is to plot the marginal PDF  $\sigma_M(m_j)$  for one parameter  $j$  (see for instance fig. 2), or the bivariate marginal PDF  $\sigma_M(m_j, m_{j'})$  (see for instance fig. 3).
- The PDF can be described by statistic indicators such as mean values (expectation), standard deviations (covariance matrix), higher order statistics, etc.

### 2.3. Monte Carlo Markov Chain (MCMC) to sample the inverse problem

Since the Hapke model is non-linear, it is not possible to describe the posterior PDF  $\sigma_M(m)$  analytically. The solution provided by Fernando et al. (2013) was to sample the final solution using a Monte Carlo approach using the Metropolis rule to built a Monte Carlo Markov chain (MCMC) (Mosegaard and Tarantola, 1995). It consists in random testing of a candidate simulation over the parameter space and keeping only some solution in order to follow the *a priori* information. After a sufficient number of steps, the chain corresponds to the desired distribution, independent of the initialization. We used a very conservative number of 500 steps.

The MCMC has been set to contain 500 sampling points. It may be not sufficient to have a smooth marginal PDF but more iterations are easy to compute using the same algorithm using more computation time. For the largest

shape in the bivariate PDF, we used 5000 sampling points instead. Let note the MCMC, sampling the final solution  $\sigma_M(m)$  as:

$$\{\tilde{m}_j\}_l, l = 1, 500 \quad (8)$$

The corresponding MCMC sampling of  $\sigma_D(d)$  is estimated using:

$$\{\tilde{r}_i\}_l = \{F(\tilde{m}_j, \Omega_i)\}_l, l = 1, 500 \quad (9)$$

Please note that this method is somehow similar to genetic algorithms (Cord et al., 2003) and Particle Swarm Optimization (Beck et al., 2012; Pommerol et al., 2013), already used to solve this inverse problem empirically. Nevertheless, those previous methods, although much faster, are only heuristic since no convergence proof of the algorithms have been proposed. This is not the case for the Metropolis rule, proposed here.

The ability to rapidly find the “best solution” of heuristic method is very convincing but these methods are not able to estimate the uncertainties. In our case, the posterior PDF of a retrieved parameter is not necessarily a gaussian distribution which is the main advantage of the Bayesian method. Nevertheless, the Metropolis method can be very slow, especially when the solution is well constrained (i.e., *a posteriori* PDF with a very low standard deviation).

In our case, all parameters have uniform physical prior distribution. If the solution has an uncertainty of 10% of the complete physical domain in  $M$  (for instance 0.5-0.6 for the parameter  $b$ , which can vary from 0 to 1), the relevant subspace in the parameter space is only  $0.1^6 = 10^{-6}$  (for 6 parameters). It means that statistically, only 1 iteration over  $10^6$  is kept in the MCMC and all other results are erased. To improve the computation time in this situation, we propose to use a fast Monte Carlo method described in section 2.5.

#### 2.4. Description of the MCMC

To describe the solution  $\sigma_M(m)$ , in addition to simple histograms, additional statistical indicators on the MCMC are proposed, following Fernando et al. (2013):

- The average value  $\hat{m}_j$  (mathematical expectation) of each parameter  $j$ , and the estimated reflectance  $\hat{r}_i$  at each geometry  $i$ .
- The covariance matrix  $\hat{C}_m$  in the model space can be estimated from the MCMC. The  $\hat{\sigma}_j$  standard deviation error bars on each parameter  $j$  are estimated from the covariance matrix elements  $\hat{C}_{mjj} = \hat{\sigma}_j^2$ .
- The non-uniformity criterion  $\hat{k}$ . The parameters  $m$  are constrained if their marginal posterior PDF differs from the prior state of information (i.e., uniform distribution in our case). In order to distinguish if a given parameter is constrained we use the non-uniformity criterion  $\hat{k}$ . Central moments  $\mu_n$  (such as the variance  $\mu_2$  at order two) are commonly used for statistical purpose while cumulants  $k_n$  have the advantage to

present unbiased statistical estimator for all orders ((Fisher, 1930)). The first four cumulants  $k_1, k_2, k_3, k_4$  of a uniform PDF are equal to  $\frac{1}{2}, \frac{1}{12}, 0, -\frac{1}{120}$ . We proposed the parameter  $\hat{k}$  to estimate the non-uniformity, defined as:

$$\hat{k} = \max \left| \frac{k_1 - \frac{1}{2}}{\frac{1}{2}}, \frac{k_2 - \frac{1}{12}}{\frac{1}{12}}, \frac{k_3}{\frac{1}{60}}, \frac{k_4 + \frac{1}{120}}{\frac{1}{120}} \right| \quad (10)$$

We perform a numerical test of 10,000 uniform random vectors of 500 samples (identical to the MCMC) and compute  $\hat{k}$  for each vectors. Since the maximum is  $\hat{k}=0.47$  for the most extreme vector, we propose to consider non-uniform PDF for  $\hat{k} > 0.5$ , which is true with a probability higher than 99.99 %. For the inversion purpose, since the a priori PDF on the parameters are uniform, if the results of the inversion on one parameter has  $\hat{k} < 0.5$ , we conclude that this parameters is not constrained by the observations.

### 2.5. Fast MCMC

The naive but accurate Monte Carlo Metropolis rule described in the previous section may be not applicable in the case of long computation time due to, either a large number of sampled geometries, or a small data uncertainty. In the first case, the computation time is large due to the time required to compute one direct model (one candidate model). In the second case, the computation time is large because the algorithm tests numerous non relevant parameter set solutions (within the model space  $M$  but far away from the actual solution).

In order to speed up the computation time, it is possible to use an adaptive Metropolis algorithm (Haario et al., 2001) but the solution (a posteriori PDF  $\sigma_M(m)$ ) has to be close to a gaussian distribution. This algorithm uses the last Markov Chain to estimate a more relevant prior information  $\rho_M(m) = \mathcal{G}(\hat{m}, \hat{C}_m)$ , recursively closer to the actual solution. If the solution is gaussian, the convergence of this method has been proven (Haario et al., 2001). Also, this method is very convenient since it reduces very significantly the number of steps. In our tests, the speedup can reach a factor 100 without significant differences, when the final solution is well constrained. Table 1 indicates an example of results on a full BRDF (see fig. 17 and 18). Differences between estimated parameters  $\hat{m}$  for MCMC and fastMCMC are always much lower than the estimated standard deviation  $\hat{\sigma}$  so we can consider as statistically equivalent.

## 3. Synthetic tests

We perform several synthetic observations in different conditions, to propagate the uncertainties from observations into the uncertainties on the Hapke parameters.

The first goal is to determine favorable geometric conditions to accurately estimate the parameters for future spaceborne, in situ and laboratory investigations (section 4). We will study two difficult cases : EPF observation and one single image / disk resolved image. The case of a full BRDF is not relevant



	algorithm	$b$	$c$	$\theta$	$\omega$	$B_0$	$h$
$\hat{m}$	MCMC	0.45	0.45	7.42	0.89	0.50	0.48
	fastMCMC	0.46	0.46	6.13	0.89	0.47	0.44
$\hat{\sigma}$	MCMC	0.06	0.08	4.30	0.02	0.28	0.29
	fastMCMC	0.04	0.06	4.57	0.02	0.30	0.27
$\hat{k}$	MCMC	1.00	1.00	0.99	1.00	0.25	0.10
	fastMCMC	1.00	1.00	1.01	1.00	0.25	0.44

Table 1: Comparison between results of the retrieved parameters  $\omega$ ,  $b$ ,  $c$ ,  $\bar{\theta}$ ,  $B_0$  and  $h$  using classical Metropolis MCMC and fast MCMC, on average value  $\hat{m}$ , standard deviation  $\hat{\sigma}$  and non uniformity criteria  $\hat{k}$ . The data is a full BRDF measurement at 96 geometrical conditions and using the following parameter set:  $b = 0.5$ ,  $c = 0.5$ ,  $\bar{\theta} = 1^\circ$ ,  $\omega = 0.9$ ,  $h = 0$ ,  $B_0 = 0$ , and 10% uncertainties as described in fig. 17 and 18. .

because the uncertainties are small for all parameters  $\omega$ ,  $b$ ,  $c$ ,  $\bar{\theta}$  with coherent values, as shown in the example in table 1. The opposition effect parameters  $B_0$  and  $h$  can only be constrained for small phase angle measurements and are out of the scope of this article. Those parameters are often studied separately in the literature.

The second goal is to estimate if the Hapke hockey stick relationship could be due to a non-linear effect on the inversion (section 5).

For each test, we compute a perfect model  $r_i$  in REFF (REFlectance Factor) unit at known geometry  $\Omega_i = (\theta_0, \theta, g)_i$  using eq. 1, and known parameter  $m_j$ . The reflectance in REFF unit is  $REFF = \pi \cdot r(\theta_0, \theta, g) / \cos(\theta_0)$ . We model the uncertainties on the measurement as a gaussian function, independent from each geometry. The standard deviation level  $\sigma_i$  at geometry  $i$  is set to 10 % of the observed reflectance  $o_i$  in all the numerical tests, except when specified:

$$\sigma_i = \frac{o_i}{10} \quad (11)$$

This value may be an upper limit for some spaceborne/laboratory instrumental uncertainties but it shall give an upper limit of the final uncertainties on the parameters. Also, taking all sources of error (including the atmosphere correction), a noise level of 10% is realistic (Ceamanos et al., 2013; Fernando et al., 2013). For the case of CRISM data, the reflectance error at each geometry were estimated at  $\sigma_i = r_i/50$  for instance (Fernando et al., 2013).

## 4. Uncertainties propagation

### 4.1. Emission Phase Function (EPF)

An Emission Phase Function (EPF) is a special configuration of observation with one particular incidence direction (incidence angle  $\theta_0$ ) and a collection of emergence angle (emergence angles  $\theta$ ) along one single azimuthal plane. Table 2 summarizes the different EPF conditions used. The EPF reflectance set, usually represented as a function of the phase angle  $g$ , is also called a photometric curve (Figure 1, black curve).

	Angular configurations
$\theta_0$ (deg.)	30 ; 40 ; 50 ; 60 ; 70 ; 80
$\theta$ (deg.) [case #1]	[70, 50, 30, 10, -10, -30, -50, -70]
$\theta$ (deg.) [case #2]	[70, 64, 58, 52, 47, 0, -47, -52, -58, -64, -70]
$\theta$ (deg.) [case #3]	[80, 70, 60, 50, 40, 30, 20, 10, 0, -10, -20, -30, -40, -50, -60, -70, -80]
$\{\varphi_1 ; \varphi_2\}$ (deg.)	$\{0 ; 180\}$ ; $\{30 ; 150\}$ ; $\{60 ; 120\}$ ; $\{90 ; 90\}$

Table 2: Angular configurations used in the EPF synthetic tests. We tested: (i) 6 incidence angles  $\theta_0$ , (ii) 3 sets of emission angle  $\theta$ . The case #1 represents a standard EPF, case #2 corresponds to a CRISM-like EPF observations and the case #3 corresponds to a favorable condition with a broad emission angle sampling typically used in laboratory investigations, (iii) 4 sets of azimuth angle  $\varphi$  ( $\varphi_1$ : azimuth angle in the illumination direction,  $\varphi_2$ : azimuth angle in the opposite illumination direction)

#### 4.1.1. Uncertainties in one EPF example

We simulate a standard EPF observations (Table 2, case #1) with a incidence angle  $\theta_0 = 60^\circ$  along the azimuthal plane  $\{\varphi_1 ; \varphi_2\} = \{30 ; 210\}$  resulting in a phase angle range from  $29^\circ$  to  $122^\circ$ , and using the following model parameter set:  $\omega = 0.9$ ,  $b = 0.8$ ,  $c = 0.1$ ,  $\hat{\theta} = 15^\circ$ ,  $B_0 = 0$  and  $h = 0$  corresponding to a bright material with a narrow forward scattering behavior and rough topographic surface. This surface corresponds to granular soil with small grain size and round shape. A similar set of parameters have been observed in the laboratory measurements of olivine at 700 nm (Souchon et al., 2011). Then, we invert the synthetic dataset with an uncertainty level set at 10% of the reflectance (one standard deviation). We examine the final solution estimated from the last 500 iterations of the Markov Chain. One have to remind that the discrepancies between the solution and the initial data are not due to the retrieval method itself, but by the lack of information in the available data (poor geometric sampling, large uncertainties).

Figure 1 presents the synthetic data and the fit of the 500 sampled solutions. The solutions are fitting the synthetic data with the expected tolerance (95% of the fits inside the  $2\sigma$  data error).

Figure 2 shows the histogram of the Hapke parameters estimated from the 500 sampled solutions. The opposition effect parameters  $B_0$  and  $h$  present a flat histogram and have a non-uniformity criterion  $\hat{k} < 0.5$ , suggesting that both parameters are not constrained. These results are directly related to the lack of observations at phase angle lower than  $20^\circ$  to observe the opposition effect. The single scattering albedo histogram shows a double peak around the expected value ( $\omega=0.9$ ), showing the effect of the Hapke model non linearity.

This example shows that the Bayesian inversion is able to identify several possible solutions due to data uncertainty and/or geometric sampling. The apparition of the double peaks on the parameter  $\omega$  has been identified to chase the limitations of geometric diversity and/or reflectance uncertainty (Fernando et al., 2013). Since, usually  $\omega$  is the best-constrained parameter in photometric modeling, the double peak in  $\omega$  is also an indicator of low-constrain on other

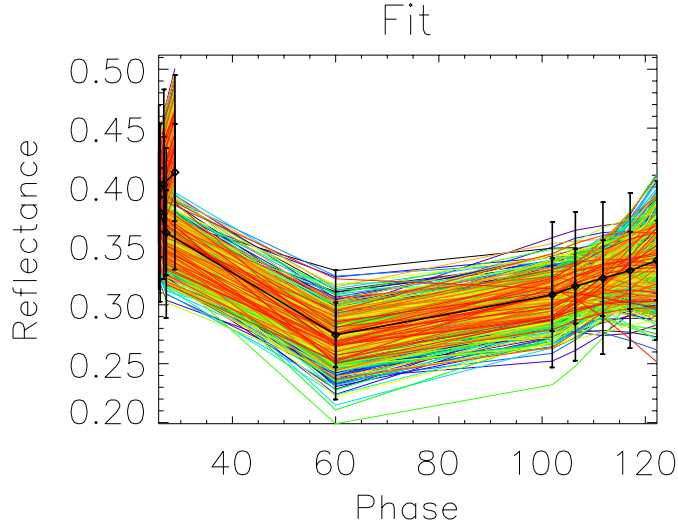


Figure 1: Example of a result on a synthetic observation with 10% uncertainty. The black curve represents the synthetic data with one and two standard deviations. Light color curves represent 500 sampled solutions from the Monte Carlo Markov Chain.

Hapke parameters. The parameters  $c$  and  $\bar{\theta}$  show a broad PDF with a maximum close to the expected solution. Interestingly, the parameter  $b$  has a PDF that is not peaking to the expected solution, most probably because the phase range  $29^\circ$  -  $122^\circ$  at 10% uncertainties is not sufficient to constrain it.

Figure 3 presents the bivariate histogram for couples of parameters, permitting to study the combined effects of two parameters. It is clearly demonstrated that all parameters are correlated. For instance, the  $b$  vs  $c$  histogram clearly shows a “U” shape covering a large part of the model space  $M$ , but with a strong correlation, excluding medium  $b$  and strong  $c$  solutions. The single scattering albedo  $\omega$  is better estimated with low  $c$  values, but higher  $c$  values are compensated by slightly lower  $\omega$ , demonstrating the complex correlation of  $\omega$  and  $c$ .

This test shows that the Bayesian inversion is able to sample complex solutions in model parameters  $M$  which is not the case for classic inversion procedures based on minimization techniques. It also demonstrates that the maximum likelihood may be a wrong indicator of the whole solution and that uncertainties may have a very complex shape due to correlation between parameters.

#### 4.1.2. Favorable geometric sampling and uncertainties

The objective of this sub-section is to evaluate the favorable geometric conditions in order to better estimate the Hapke photometric parameters by simulating various surface scattering properties. These tests allow to evaluate the influence of the EPF geometric sampling in the uncertainties of the retrieved

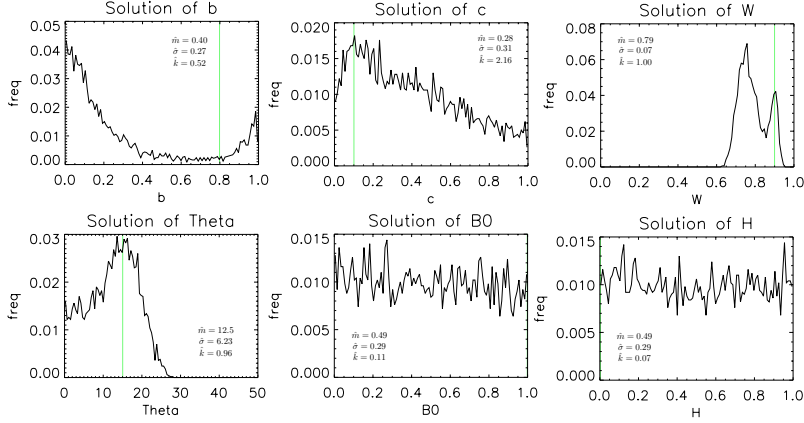


Figure 2: Probability Density Function (PDF) of the solution, for each parameter of the Hapke model on the same example as fig. 1. Each plot represents the histogram of the 500 acceptable solution from the Monte Carlo Markov Chain. The color line represent the initial parameters set.

model parameters. These synthetic results should give constraints for current spaceborne data analyses (e.g., CRISM/MRO, HRSC/MRO, OMEGA/MEx for Mars, VIMS/Cassini for Titan, VIRTIS/Rosetta for 67P/Churyumov-Gerasimenko, LROC/LRO for the Moon, etc) and future instrumental and laboratory investigations. The following tests are done only for realistic soil cases, with  $b/c$  in the Hapke hockey-stick relationship. The opposition effect is not studied here because it is usually investigated separately from the global photometric data, this effect being only rarely observable in spaceborne data.

We perform synthetic tests, using various surface scattering properties in order to cover the range of properties which can be observed in natural environments (i.e., different Hapke parameter sets):

- 2 single scattering albedos ( $\omega$ ): 0.3; 0.9
- 6 parameters ( $b$  and  $c$  couples) taken along the hockey stick relation: L1( $b=0.3/c=1.0$ ), L2(0.3/0.8), L3(0.3/0.5), L4(0.5/0.2), L5(0.8/0.1), L6(0.8/0.1)
- 2 macroscopic roughnesses ( $\bar{\theta}$ ):  $0^\circ$  ;  $15^\circ$
- Opposition effect parameters are set to ignore this effect:  $B_0=0$  and  $h=0$ .

We perform the synthetic tests under various geometric configurations summarized in Table 2: 6 incidence angles, 4 azimuthal modes and 2 cases of emission angles samplings where the case #2 to a CRISM-like EPF observation with a poor-sampling and a narrow emission angle range (11 configurations) and the case #3 corresponds to a EPF with a well-sampling and broad emergence angle range (17 configurations). In what follows, we focus on the results of the

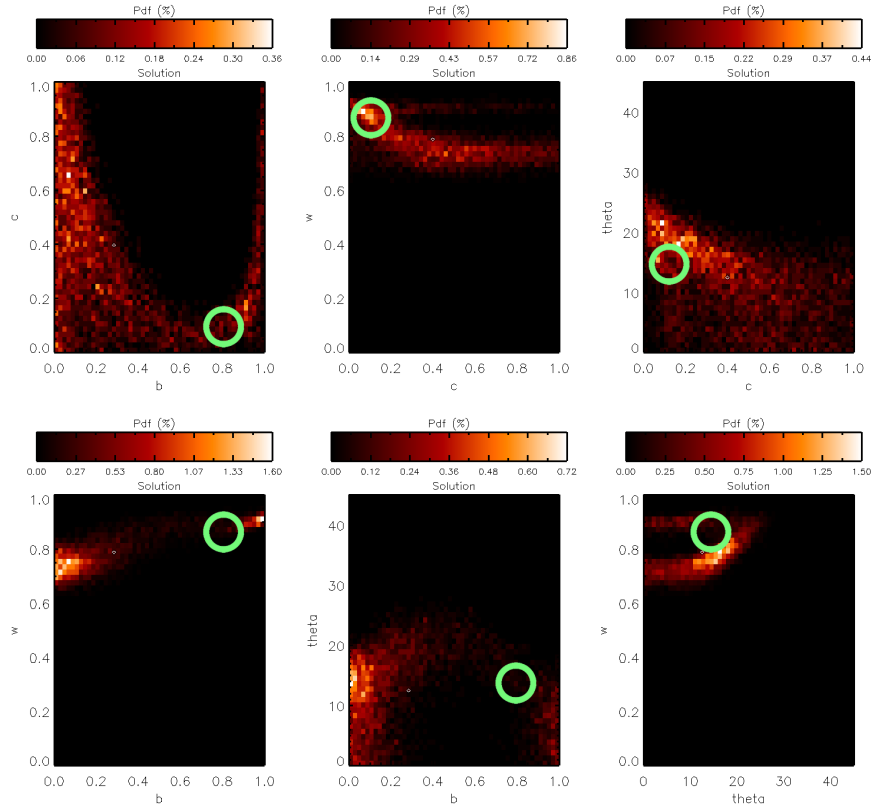


Figure 3: Probability Density Function (PDF) of the solution, for each couple of constrained parameters  $(\omega, b, c, \theta)$  on the same example as fig. 1 and 2. The black/white diamonds represent the average of the PDF. The green circles represent the expected values for each parameter.

case #2 as for example but all the results of the case #3 are presented in the Supplementary Materials.

All 576 configurations are summarized in a single graph by computing the difference between initial parameter value of the synthetic test  $m_j$  and the estimated one from the Bayesian inversion  $\tilde{m}_j$  (with  $j$  the index of parameter and  $l$  the index of the Markov Chain):

$$\{\Delta m_j\}_l = \{\tilde{m}_j\}_l - m_j \quad (12)$$

This quantity represents the deviation between the initial “true” parameters and the state of information present in the EPF data, given the geometric sampling and uncertainties. The histogram of  $\{\Delta m_j\}_l$  represents the PDF of uncertainties. By tracing marginal PDF, it is possible to chase the effect of each parameter on the uncertainties. One has to remind that the deviation between the solution and the initial value are not due to the retrieval method itself, but to the lack of information in the available dataset.

Figures 4 to 8 present the deviation for one studied parameter each: geometric configurations: incidence angles (fig. 4), azimuthal modes (fig. 5), model parameter:  $c$  and  $b$  couple (L1 to L6) (fig. 6),  $\omega$  (fig. 7) and  $\bar{\theta}$  (fig. 8) by averaging the effects of all other parameters. The results show that the distributions of  $\{\Delta m_j\}_l$  are always maximum on 0, showing that the maximum likelihood is globally unbiased. It demonstrates that a single EPF is enough to estimate accurate model parameters in most of the cases.

Nevertheless, the pick and the tails shape of the PDF of uncertainties are not identical for all marginal probabilities, showing that the CRISM-like EPF sampling can be optimized for some geometries, or for some surface parameters.

One has to note that the roughness parameter is tested for the case  $\bar{\theta} = 0$ . Since  $\theta \geq 0$  by definition, the deviation cannot be symmetrical ( $\{\Delta m_j\}_l \geq 0$ ), this significantly biases the deviation PDF.

In detail, we can take the following conclusions:

- The single scattering albedo parameter  $\omega$  presents the narrower deviation PDF in comparison to other Hapke parameters (fig. 4 to 8 ). Thus  $\omega$  is the best constrained parameter on EPF measurement.
- The influence of the geometric sampling on the deviation is very important: both incidence angle (fig. 4) and azimuthal mode (fig. 5) significantly change the global uncertainties:
  - Incidence has a strong effect on the estimation of surface roughness: the larger the incidence, the better the estimation of  $\bar{\theta}$ .
  - Azimuth has a strong effect on  $b$ ,  $c$  and  $\omega$ : the closer to principal plane, the better the estimation. This effect is also present on  $\bar{\theta}$  but more moderately.
  - We can interpret this behavior by the diversity of phase angles necessary to constraint the photometric parameters, both at low ( $g < 30^\circ$ ) and high ( $g > 100^\circ$ ) ranges. Observations acquired at high incidence

angles and/or close to the principal plane allow to have the broadest phase angle ranges corresponding to the most favorable conditions. A departure from principal plane as low as  $30^\circ$  leads to significant increase of the uncertainties.

- The influence of the model parameter values on deviation play a second order role:
  - The phase function parameters seem to have a strong influence on the retrieved parameters. In particular, the parameters  $b$ ,  $c$  and  $\omega$  are significantly better estimated for surface materials with a narrow forward behavior (e.g., L6) (fig. 6).
  - The single scattering albedo  $\omega$  has a moderate effect on the estimation of the parameters  $c$  and  $\omega$ : (i) the estimation of parameter  $\omega$  is better when the albedo is high, (ii) the estimation of the parameter  $c$  is better when the albedo is lower (fig. 7).
  - The macroscopic roughness  $\bar{\theta}$  has a small effect on the estimation of the parameters  $b$ ,  $c$  and  $\omega$ : the parameter estimations are better when the parameter  $\bar{\theta}$  is lower. (fig. 8).
- Those conclusions are also valid for the case of favorable EPF (case #3, presented in the Supplementary Materials), except that the uncertainties are slightly reduced in this case.

A similar study has been proposed on one experimental dataset using the genetic algorithm (Souçon et al., 2011). The authors recommended a “regular coverage of the bidirectional space in incidence, emission, azimuth, and consequently phase angles” and showed that “reliable photometric estimates can be produced with a limited set of angular configurations (on the order of a few tens)”. Our conclusions demonstrate that this experimental work can be extended even in the principal plane when large phase angle range are available.

#### 4.2. One single observation of a rough surface / disk resolved image

One single image of a known rough surface has very limited angle geometry. Such observational condition corresponds to the case where each pixel of the image is assimilated to a facet with known orientation. We assume that the surface properties are spatially homogeneous over a large amount of pixel in order to estimate the surface properties by combining several adjacent pixels. This case is equivalent to a disk resolved measurement of a planetary body assumed to be homogeneous in surface properties, at one single phase image. We study this very difficult condition, in order to estimate if it is possible to constrain the photometric parameters.

For each facet (or equivalently for each image pixel), the incident and emergent rays are parallel, with the same phase angle. However, since each facet has its own orientation, there is a variability of local incidence, emergence and azimuth angles. We propose to use a typical observation condition of incidence

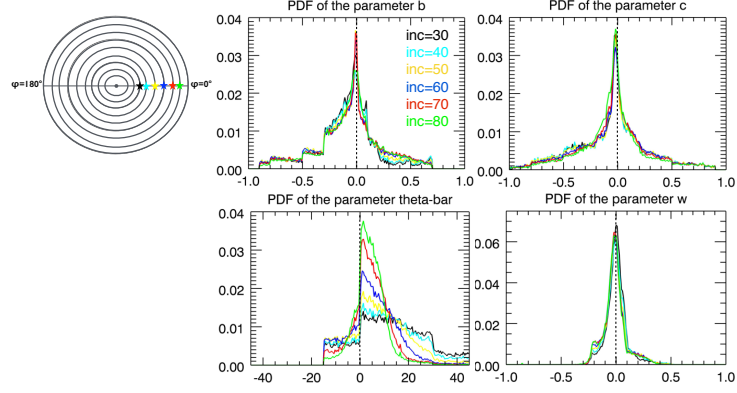


Figure 4: Difference between true parameter and the Bayesian solution (see eq. 12), for 6 incidence:  $30^\circ$ ,  $40^\circ$ ,  $50^\circ$ ,  $60^\circ$ ,  $70^\circ$ ,  $80^\circ$ . All other parameters are included.

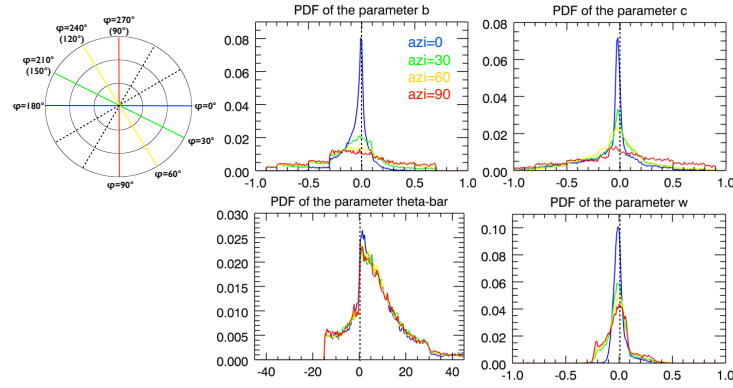


Figure 5: Difference between true parameter and the Bayesian solution (see eq. 12), for 4 azimuth:  $0^\circ$ ,  $30^\circ$ ,  $60^\circ$ ,  $90^\circ$ . All other parameters are included.



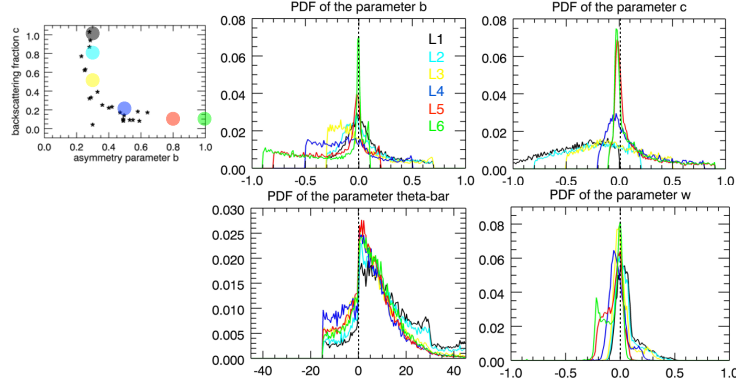


Figure 6: Difference between true parameter and the Bayesian solution (see eq. 12), for 6 configurations of phase function parameters in the hockey stick: #1( $b=0.3/c=1.0$ ), #2( $0.3/0.8$ ), #3( $0.3/0.5$ ), #4( $0.5/0.2$ ), #5( $0.8/0.1$ ), #6( $0.8/1.0$ ). All other parameters are included.

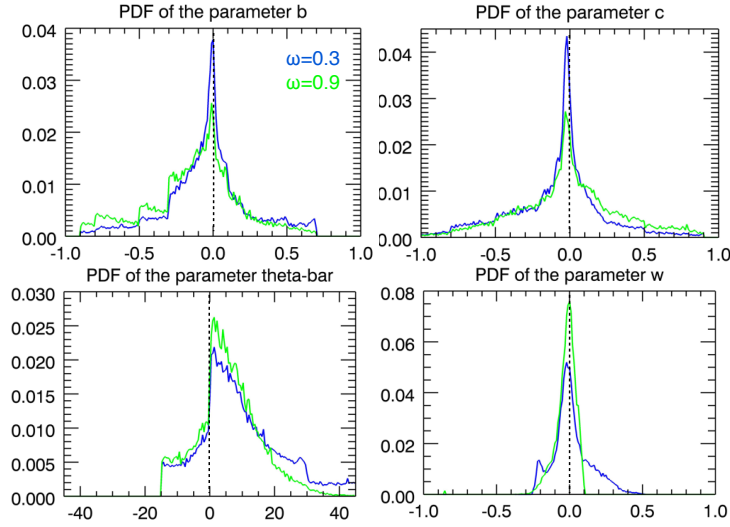


Figure 7: Difference between true parameter and the Bayesian solution (see eq. 12), for 2 single scattering albedo  $\omega$ : 0.3, 0.9. All other parameters are included.

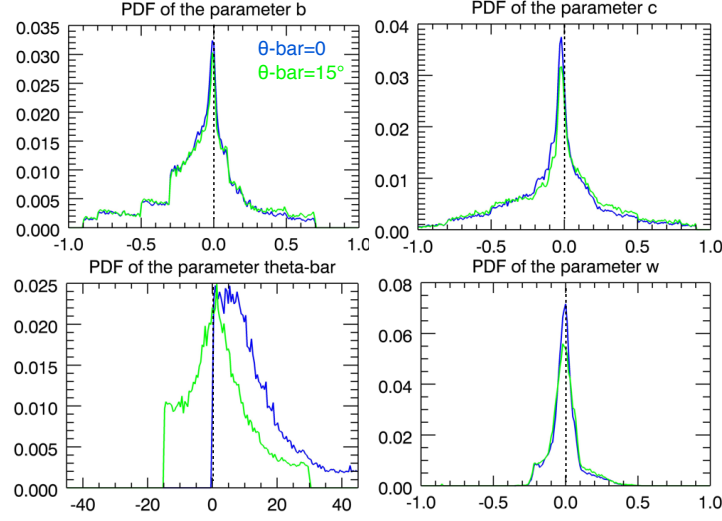


Figure 8: Difference between true parameter and the Bayesian solution (see eq. 12), for 2 macroscopic roughness  $\bar{\theta}$ :  $0^\circ$ ,  $15^\circ$ . All other parameters are included.

$\theta_0 = 40^\circ$ , emergence  $\theta = 0^\circ$  on 24 facets with 6 slopes  $\theta_s = 5^\circ, 10^\circ, 20^\circ, 30^\circ, 40^\circ, 50^\circ$  and 4 azimuth of slope  $\phi_s = 0^\circ, 90^\circ, 180^\circ, 270^\circ$ . Each facet is thus defined by a couple of slope and azimuth angles  $(\theta_s, \phi_s)$ . The phase angle is always  $g = 40^\circ$ , but the local incidence  $\tilde{\theta}_0$  on the facet varies from  $0^\circ$  to  $90^\circ$ , the local emergence  $\tilde{\theta}$  from  $5^\circ$  to  $50^\circ$  and the local azimuth  $\tilde{\phi}$  from  $0^\circ$  to  $180^\circ$ . The relationship between slopes, azimuth of slopes and local incidence and emergence are the following Hapke (1993):

$$\cos \tilde{\theta}_0 = \cos \theta_0 \cos \theta_s + \sin \theta_0 \sin \theta_s \sin \phi_s \quad (13)$$

$$\cos \tilde{\theta} = \cos \theta \cos \theta_s + \sin \theta \sin \theta_s \sin \phi_s \quad (14)$$

We test  $\omega = 0.9$ ,  $\bar{\theta} = 1^\circ$  and three values of the  $b/c$  in the hockey stick : #1( $b=0.3/c=1.0$ ), #4( $0.5/0.2$ ), #6( $1.0/0.1$ ).

The results are plotted in figure 9, in terms of bi-variate histograms describing  $b$  vs  $c$ , and  $\omega$  vs  $\bar{\theta}$ . The parameter  $\omega$  seems to be well constrained in all cases but the parameter  $\bar{\theta}$  is only constrained in the case of a strong narrow forward scattering. The particulate phase function parameters  $b$  is only constrained in the extreme cases of the hockey stick (cases #1 and #6). The parameter  $c$  is not constrained.

These results indicate that information of the surface properties can be retrieved even in the case of one single observation with known geometry for each facet. Especially  $\omega$  can be retrieved with small uncertainties ( $1\sigma$  uncertainties  $\leq 0.1$ ), but also  $b$ ,  $c$  and in some extent  $\bar{\theta}$ , in the case of very extreme phase function.

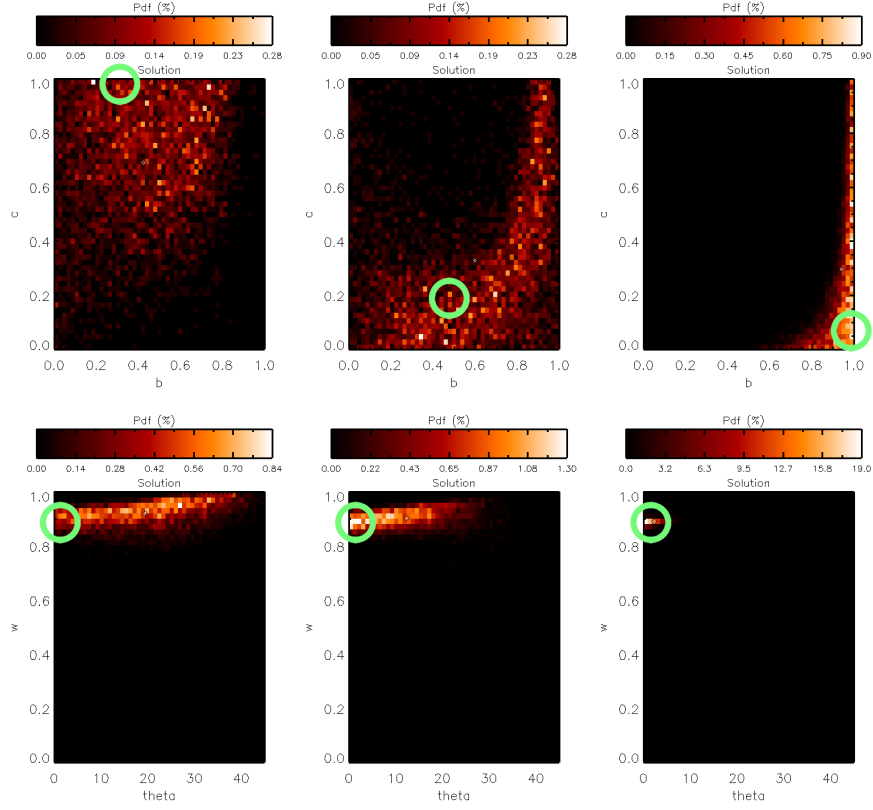


Figure 9: Probability Density Function of the solution, for each couple of constrained parameters ( $\omega$ ,  $b$ ,  $c$ ,  $\bar{\theta}$ ) derived from the simulation of a single observation of a known rough surface with 24 facets (see the text for more detail). At the left case #1( $b=0.3/c=1.0$ ). In the middle, case #4( $0.5/0.2$ ). At right case #6( $1.0/0.1$ ). The black/white diamonds represent the average calculated from of the PDF. The green circles represent the expected values for each parameter.

## 5. Possible origin of the hockey stick relationship

We exhibit here particular conditions of Emission Phase Function (EPF) and Bidirectional Reflectance Distribution Function (BRDF) that could be a possible bias at the origin of the hockey stick relationship, so we focus in this section on the parameters  $b$  and  $c$ . We set  $\omega=0.9$ ,  $\bar{\theta} = 1^\circ$ ,  $h=0$ ,  $B_0=0$  and data uncertainties at a level of 10% as previously defined. The results are expected to be only weakly dependent of  $\omega$  and  $\bar{\theta}$  (see section 4.1.2). These surface properties correspond to granular soil with small grain size. Similar parameters have been observed in sulfate terrain on Mars (Johnson et al., 2006a), and in various samples (Souchon et al., 2011), such basalt including feldspar grains, pyroclastic grains and olivine grains.

We test here all configurations of  $b/c$  covering the whole parameter spaces from 0 to 1 and see if the resulting uncertainties can bias the interpretation or not. We insist on the fact that materials with both  $b \geq 0.5$  and  $c \geq 0.5$  have never been observed. Nevertheless, we tested these configurations in order to study the potential bias when analyzing such case.

### 5.1. Principal plane EPF

Figure 10 presents the results for a standard principal plane EPF observation (Table 2 case #1) (i.e. poor-sampling of emission angles, mostly the case for spaceborne instruments like CRISM). It shows that low  $b$  ( $< 0.5$ ) imply poor constraint on  $c$  and very large uncertainties on  $b$ . For  $b \geq 0.5$  and  $c \geq 0.5$ ,  $b$  has small uncertainties and  $c$  has medium uncertainties.

Figure 11 presents the results for a favorable principal plane EPF observation (i.e., well sampling of emission angles which can be obtained at laboratory, on in situ in very favorable conditions). The solution is clearly better constrained than for the standard principal plane (see fig. 10). It demonstrates that even at 10% data uncertainties, the correct behavior (backward/forward and narrow/broad) can be retrieved from a single EPF observation if the observation is taken in or close to the principal plane.

### 5.2. Effect of azimuth on EPF

Figures 11, 12, 13, 14 and 15 present the results of the favorable EPF with an azimuthal plane, respectively  $\{0^\circ, 180^\circ\}$ ,  $\{30^\circ, 210^\circ\}$ ,  $\{45^\circ, 225^\circ\}$ ,  $\{60^\circ, 240^\circ\}$ ,  $\{90^\circ, 270^\circ\}$ . As expected, the information included in one EPF observation to constrain the parameters  $b$  and  $c$  is decreasing by increasing the azimuthal plane angle. At an azimuthal plane angle of  $0^\circ$  (principal plane, shown in fig. 11), the solutions are well constrained when the parameter  $b$  value is greater or equal 0.5 as observed in section 5.1. At an azimuthal plane angle as low as  $30^\circ$  (Figure 12), the solution is not well constrained in most cases, except for the cases when  $b=0.5$  and the case when  $b=0.9$  and  $b=0.1$ . At an azimuthal plane angle of  $90^\circ$  (Figure 15), only the parameter  $b$  can be qualitatively estimated (i.e., by discriminating the broad and the narrow scattering), the parameter  $c$  is unconstrained (i.e., all the solutions for the parameter  $c$  are possible), because

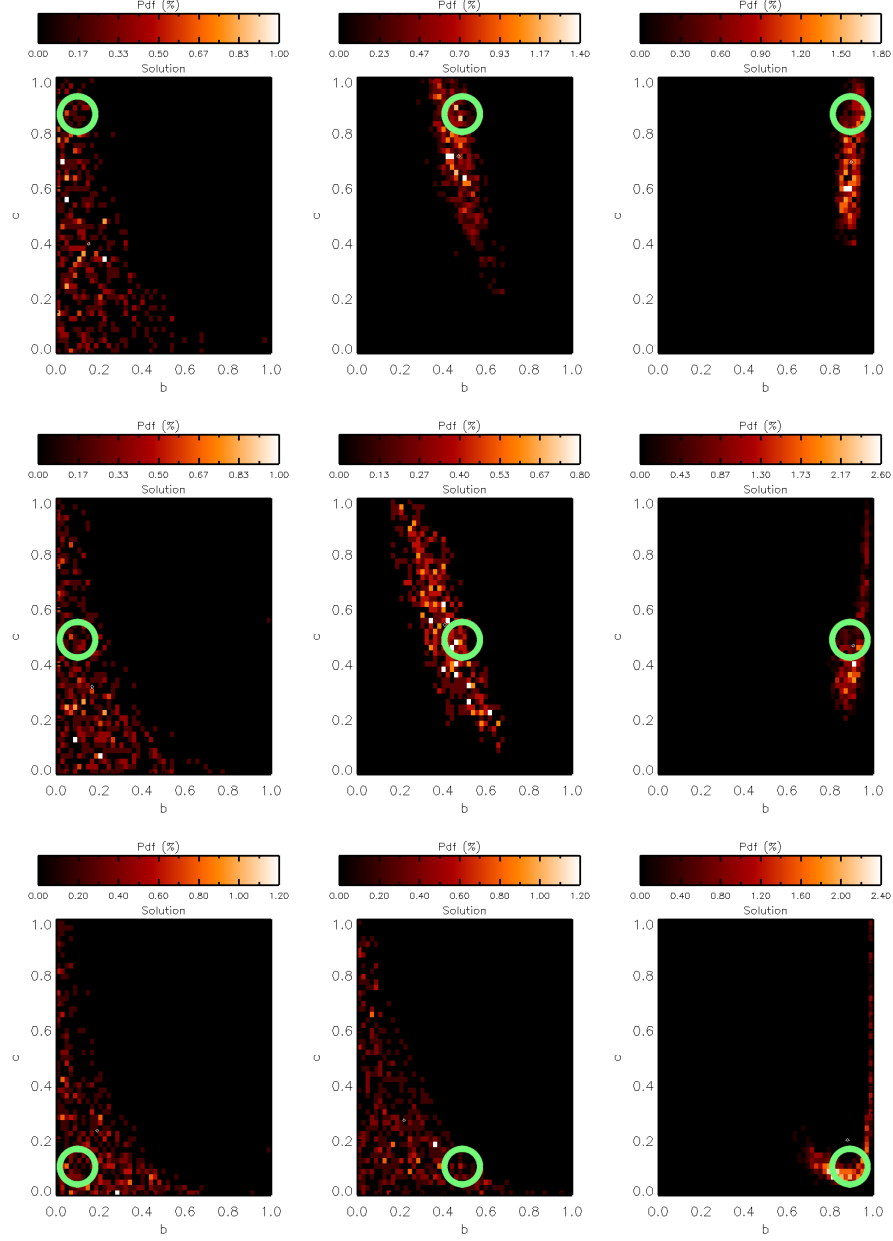


Figure 10: Probability density function of the  $b$  and  $c$  parameters using a standard principal plane EPF observation (8 emergence configurations:  $70^\circ$ ,  $50^\circ$ ,  $30^\circ$ ,  $10^\circ$ ,  $-10^\circ$ ,  $-30^\circ$ ,  $-50^\circ$ ,  $-70^\circ$ ), incidence= $40^\circ$ , azimuth= $\{0, 180^\circ\}$  and using the following parameter set:  $\omega=0.9$ ,  $\bar{\theta} = 1^\circ$ ,  $h=0$ ,  $B_0=0$ , data uncertainties 10% and 9 combinations of  $b=0.1/0.5/0.9$  and  $c=0.1/0.5/0.9$ . The black/white diamonds represent the average of the PDF. The green circles represent the expected values of the parameters  $b$  and  $c$ .

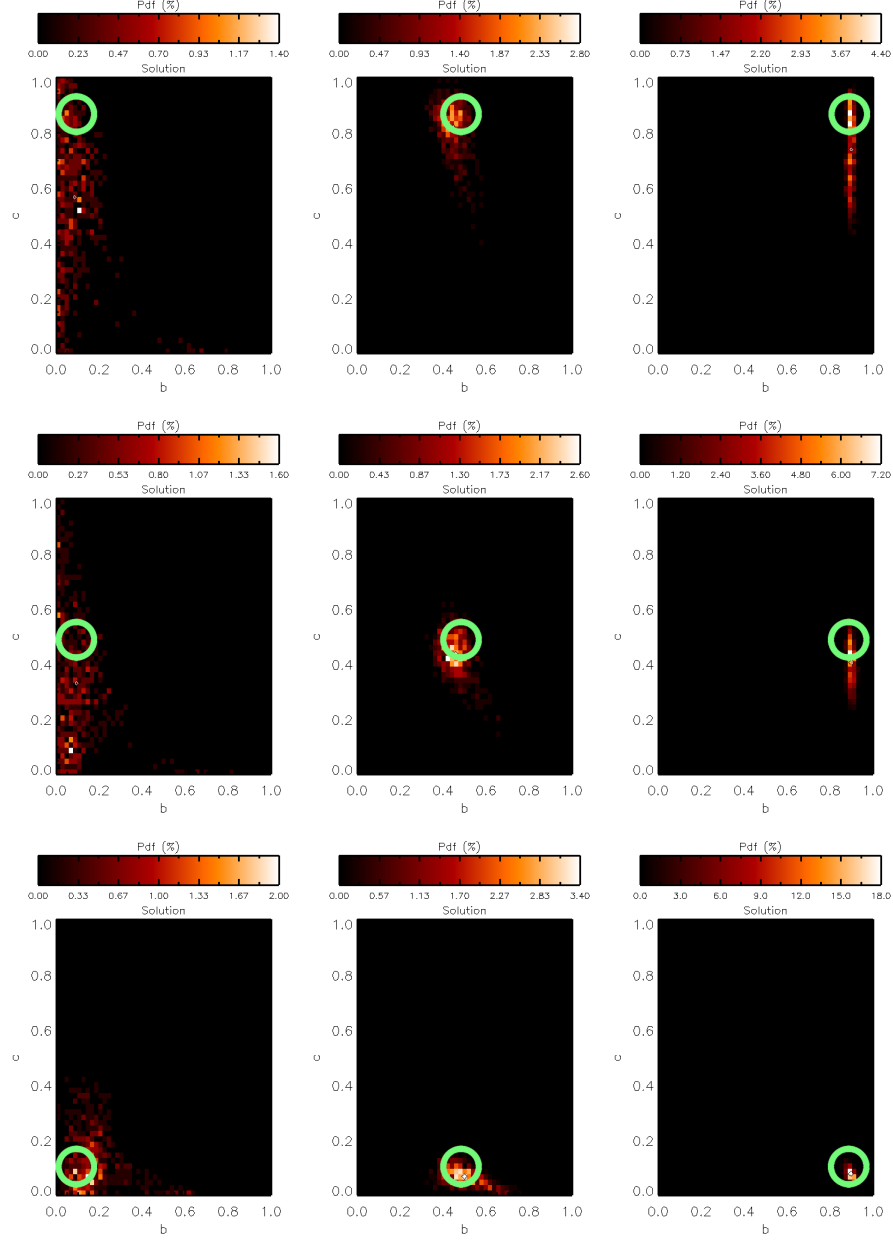


Figure 11: Probability density function of the  $b$  and  $c$  parameters using a favorable principal plane EPF observation (17 emergence configurations:  $80^\circ, 70^\circ, 60^\circ, 50^\circ, 40^\circ, 30^\circ, 20^\circ, 10^\circ, 0^\circ, -10^\circ, -20^\circ, -30^\circ, -40^\circ, -50^\circ, -60^\circ, -70^\circ, -80^\circ$ ), incidence= $75^\circ$ , azimuth= $\{0, 180^\circ\}$  and using the following parameter set:  $\omega=0.9$ ,  $\theta=1^\circ$ ,  $h=0$ ,  $B_0=0$ , uncertainties 10% and 9 combinations of  $b=0.1/0.5/0.9$  and  $c=0.1/0.5/0.9$ . The black/white diamonds represent the average of the PDF. The green circles represent the expected values of the parameters  $b$  and  $c$ .

no phase angles greater than  $90^\circ$  are available in the data, very important to distinguish the forward and the backward scattering direction.

Interestingly, the behavior of a high  $b$  value coupled with moderate to high  $c$  value differs from the other cases: a “U” shape solution is expressed only in this quadrangle. If the tool used for the inversion is based on a root mean square minimization, it clearly depends on the initialization. If the initialization is in the hockey stick shape, it would converge to a fake local maximum. This effect may be a significant bias on the estimation of the parameters  $b$  and  $c$ , leading to an artificial hockey stick effect, present for EPF data with azimuthal plane larger than  $30^\circ$  and inappropriate inversion method.

### 5.3. Effect of noise level on EPF

In order to test the noise level on the retrieved parameters, we vary the noise level (eq. 11), from 50% to 1%. First, figure 16 clearly shows that with 50% data uncertainty, all solutions in the parameters  $b$  and  $c$  spaces are possible, thus the parameters are not constrained due to the large data uncertainty. With 10% data uncertainty, the solution is only restricted to the “U” shape leading to the artificial hockey-stick like shape. The  $b$  and  $c$  couple can be correctly evaluated with a data uncertainty lower than 5%. Such uncertainty level can often be obtained in laboratory measurements (Pommerol et al., 2013; Johnson et al., 2013) but sometimes also in spaceborne measurements (Fernando et al., 2013). Finally with 1% data uncertainty, the solution is well constrained close to the expected solutions.

The artificial hockey stick effect discussed in the previous section is only present for uncertainties larger than 5-10%.

### 5.4. Full BRDF

We test the BRDF observation, sampled 48 times at 2 incidence angles  $40^\circ$  and  $60^\circ$ , 8 emergence angles:  $70^\circ$ ,  $50^\circ$ ,  $30^\circ$ ,  $10^\circ$ ,  $-10^\circ$ ,  $-30^\circ$ ,  $-50^\circ$ ,  $-70^\circ$  and 3 azimuth angles:  $0^\circ$ ,  $45^\circ$  and  $90^\circ$ . This sampling corresponds to the combination of standard EPF (table 2, case #2) for 3 azimuthal plane angles,  $0^\circ$ ,  $45^\circ$ ,  $90^\circ$  and two incidence angles, allowing high diversity of geometries. It represents typical laboratory measurements or the best expected combination of single EPF on the same site. Such combination of EPF have already been proposed in the literature (Jehl et al., 2008; Fernando et al., 2013; Fernando et al., 2015).

The results, presented in fig. 17, show that the BRDF configuration contains enough information to constrain the parameters  $b$  and  $c$ , in comparison with single EPF (fig. 10) with lower uncertainties. Interestingly, the favorable EPF condition (fig. 11) is able to better constrain the phase function parameters than the standard BRDF presented here. This effect is most probably due to the maximum phase angle that is limited to  $130^\circ$  for the BRDF considered here but goes to  $155^\circ$  for the favorable EPF.

A full BRDF observation at 10% uncertainties is able to constrain the parameters  $b$  and  $c$ , and should reduce the contribution to the hockey stick artifact.

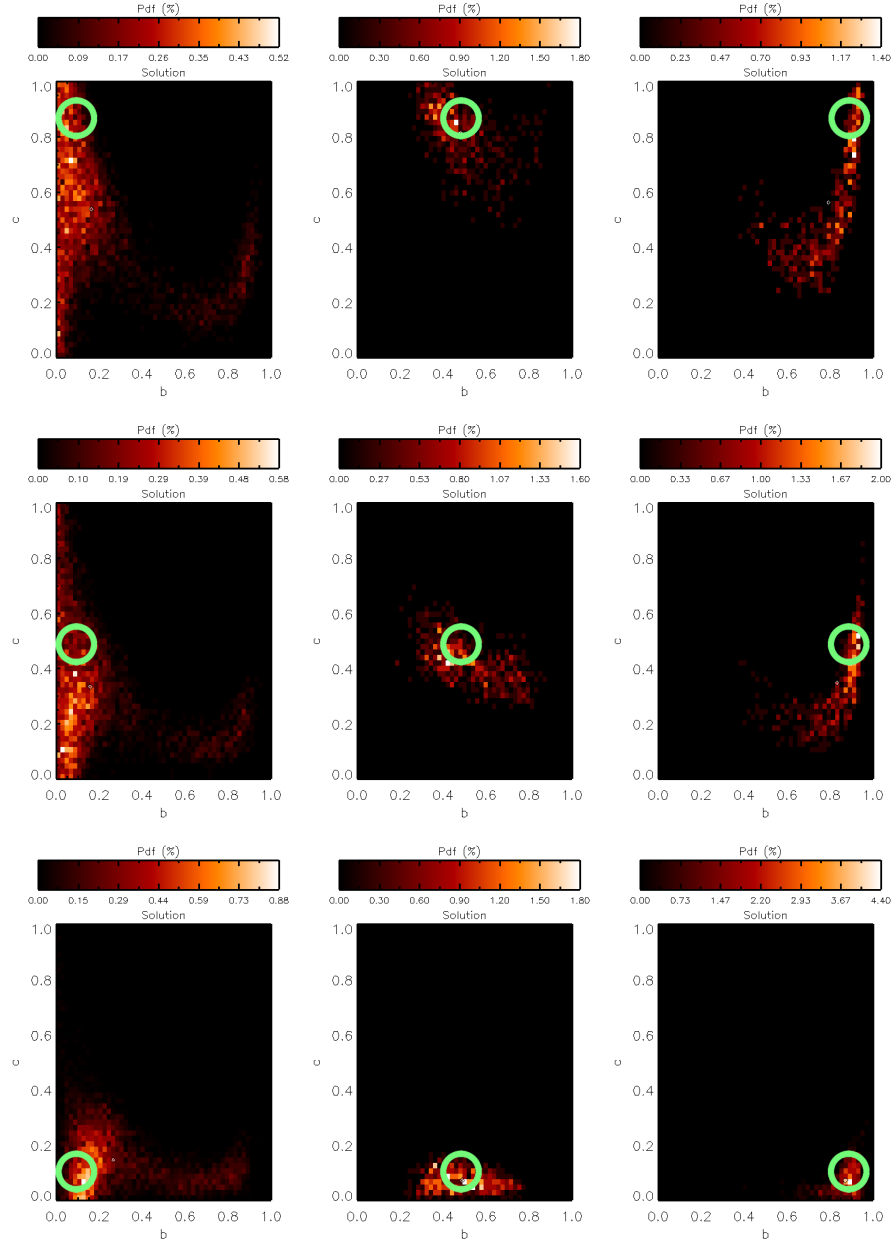


Figure 12: Same as fig. 11 but with  $\text{azimuth}=\{30^\circ, 210^\circ\}$ .



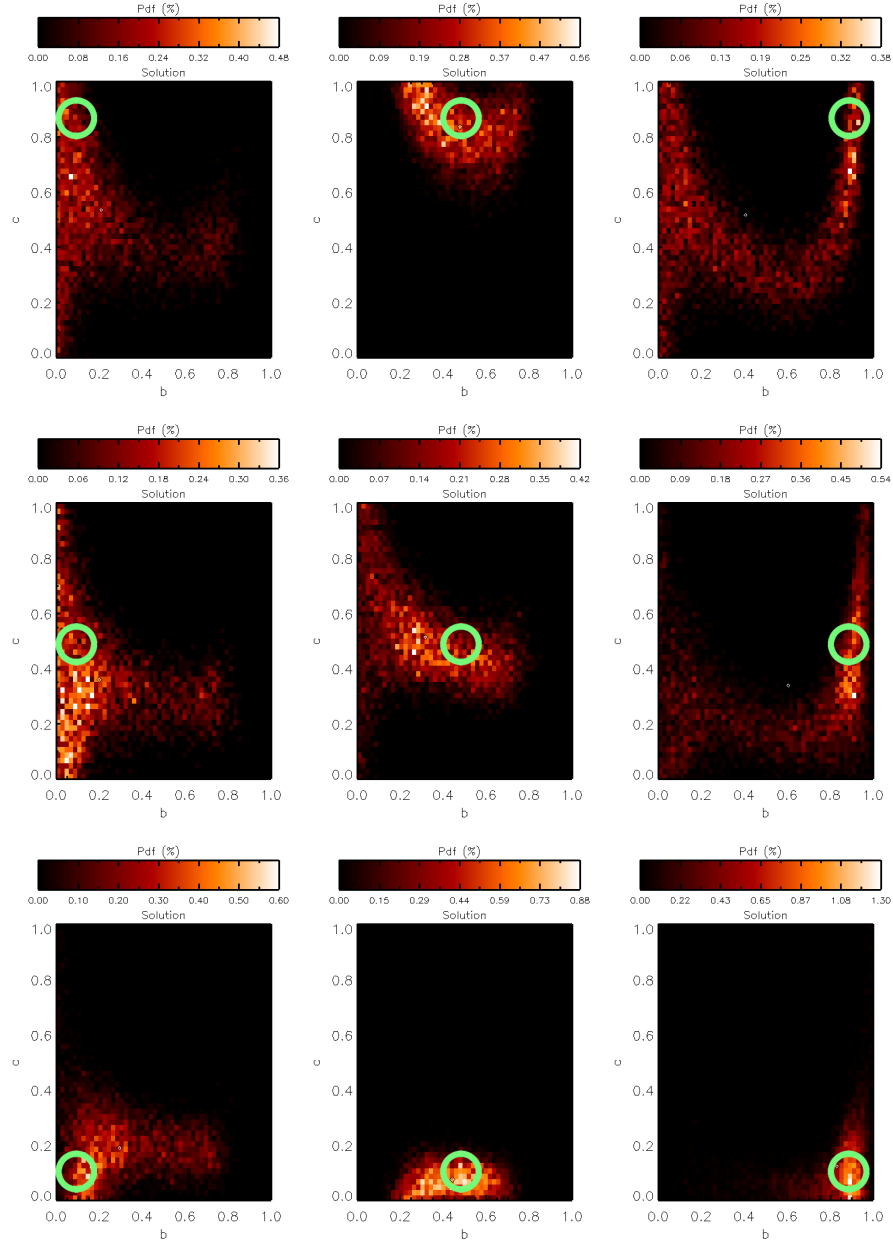


Figure 13: Same as fig. 11 but with  $\text{azimuth}=\{45^\circ, 225^\circ\}$ .

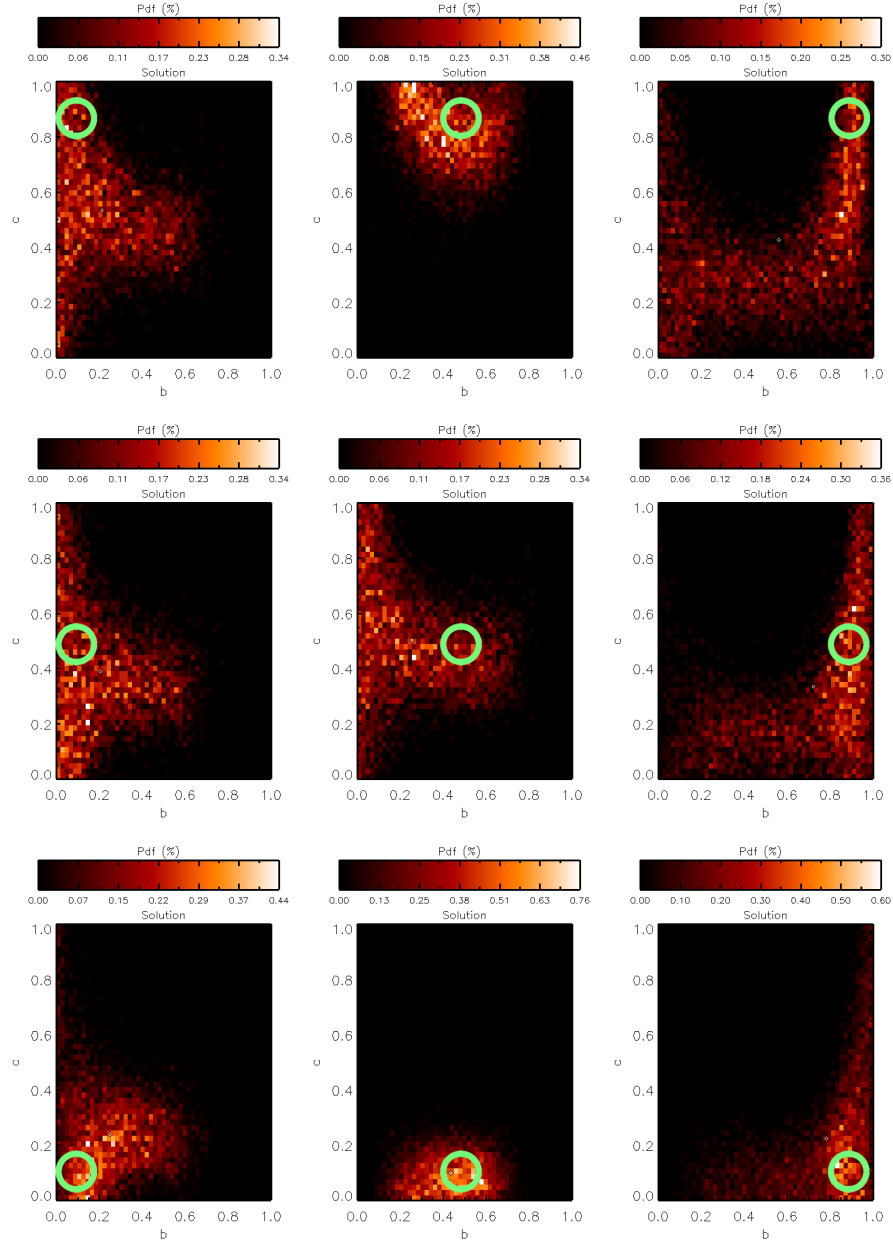


Figure 14: Same as fig. 11 but with azimuth= $\{60^\circ, 240^\circ\}$ .

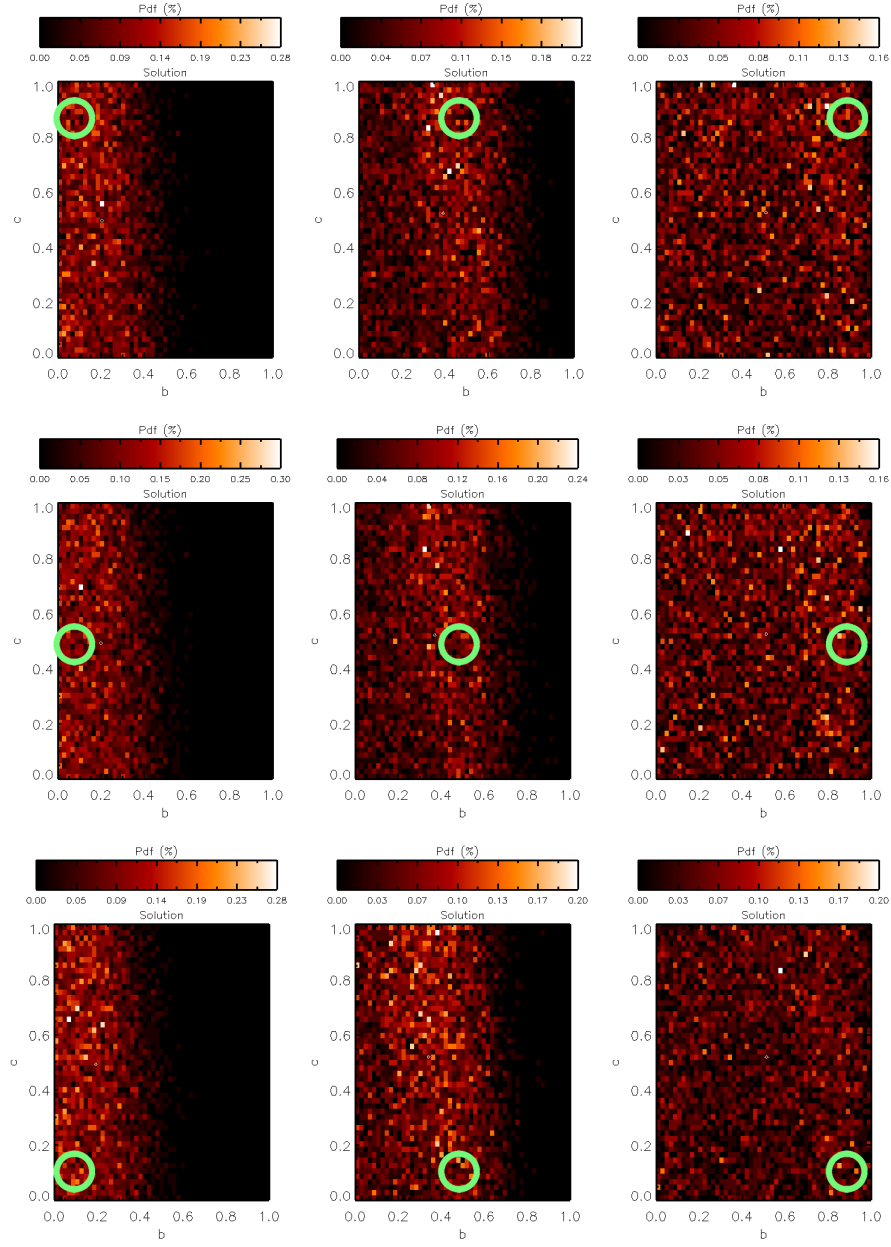


Figure 15: Same as fig. 11 but with azimuth= $\{90^\circ, 270^\circ\}$ .

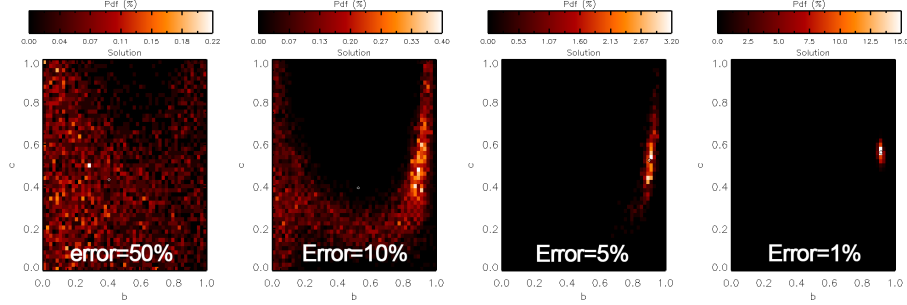


Figure 16: Probability density function of the parameter  $b$  and  $c$  using a favorable EPF observation (17 emergence configurations:  $80^\circ, 70^\circ, 60^\circ, 50^\circ, 40^\circ, 30^\circ, 20^\circ, 10^\circ, 0^\circ, -10^\circ, -20^\circ, -30^\circ, -40^\circ, -50^\circ, -60^\circ, -70^\circ, -80^\circ$ ), incidence= $75^\circ$ , azimuth= $\{45^\circ, 225^\circ\}$  and using the following parameter set:  $\omega=0.9$ ,  $\bar{\theta} = 1^\circ$ ,  $h=0$ ,  $B_0=0$ ,  $b=0.9$  and  $c=0.6$ . Different uncertainties values are tested: 50%, 10%, 5%, 1%. The black/white diamonds represent the average of the PDF.

## 6. Discussions and Conclusion

We proposed a rigorous inversion scheme to estimate Hapke model parameter from measurements, using Bayesian Monte Carlo strategy. The typical computation time on a 2.5 GHz Intel Core I5, 8Go RAM, is one minute for a single EPF but can reach one hour for a BRDF. In order to speed up the convergence, we developed a Fast Monte Carlo strategy, reducing the computation time by a factor of 100. This strategy is only suitable on full BRDF or favorable EPF, when gaussian like solutions are expected.

We explored various conditions on synthetic examples: EPF type observations, one single observation, BRDF type observations in order to study the propagation of errors from measurements to the parameter space with 10% uncertainties as a nominal condition. The major conclusions of this work are:

- Non-linearities in the Hapke model are important for EPF type measurements leading to potential multiple solutions, at least with data uncertainties larger than 5% and large azimuthal plane angle ( $> 30^\circ$ ).
- Azimuthal plane in a EPF observation is the most important parameter to constrain the photometric parameters: the closer to the principal plane, the best the results. A departure of only  $30^\circ$  in azimuthal plane leads to significant increase of uncertainty.
- Incidence angle is very important to constrain the parameters in a EPF, especially the roughness parameter  $\bar{\theta}$ . A recommendation for laboratory or spaceborne observation is to sample the highest incidence angle possible.
- One single EPF type observation with very favorable conditions (i.e., principal plane, incidence at  $75^\circ$ , emergence angle sampling up to  $80^\circ$ ) is enough to constrain  $\omega$ ,  $b$ ,  $c$ , and  $\bar{\theta}$  parameters, even with a data uncertainty level of 10%.

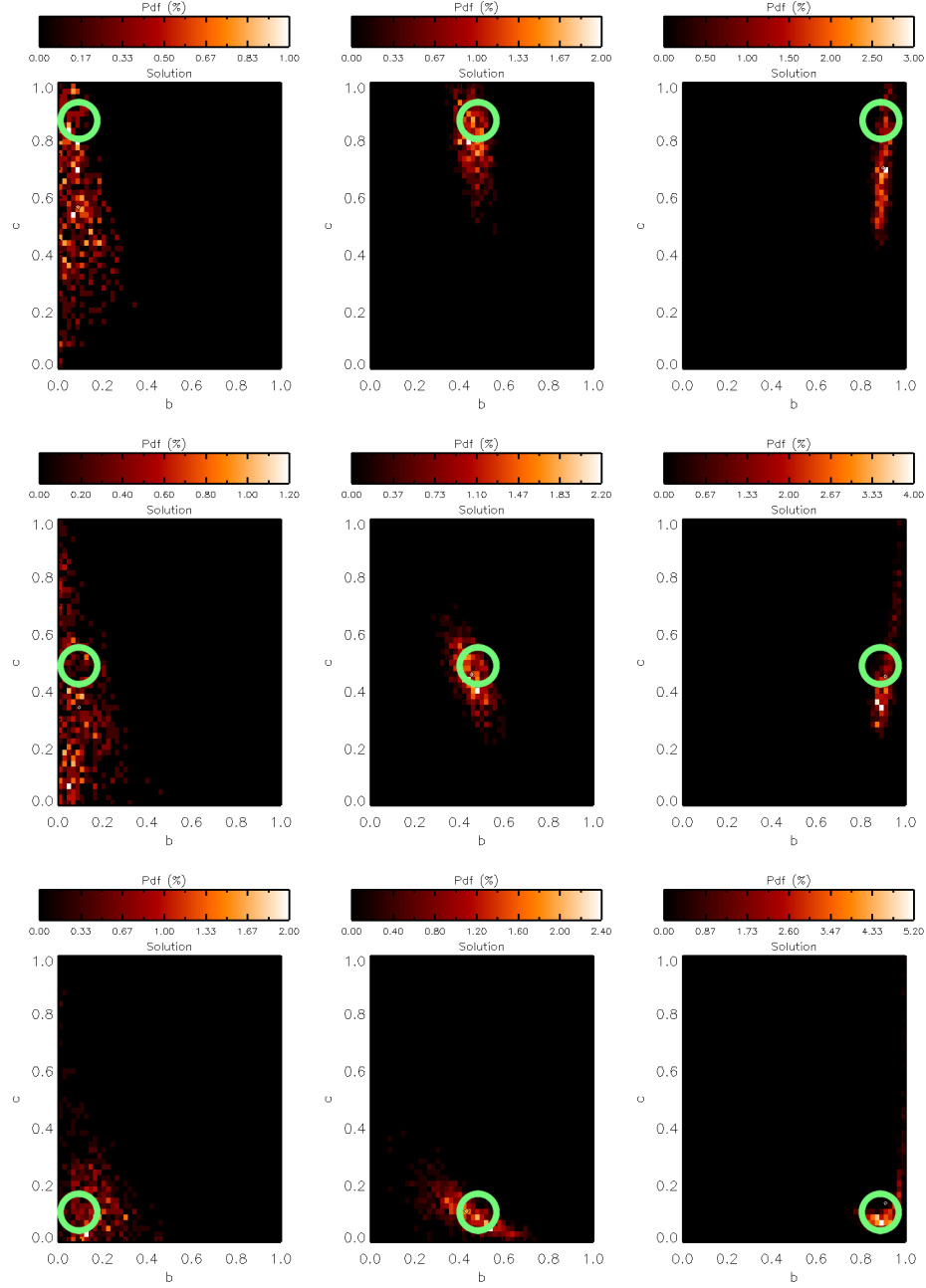


Figure 17: Same as fig. 10 but for a full BRDF observation including 48 geometries (2 incidence angles:  $40^\circ$  and  $60^\circ$ , 8 emergence angles:  $70^\circ$ ,  $50^\circ$ ,  $30^\circ$ ,  $10^\circ$ ,  $-10^\circ$ ,  $-30^\circ$ ,  $-50^\circ$ ,  $-70^\circ$  along 3 azimuth angles:  $0^\circ$ ,  $45^\circ$ ,  $90^\circ$  and using the following parameter set:  $\omega=0.9$ ,  $\bar{\theta}=1^\circ$ ,  $h=0$ ,  $B_0=0$ , data uncertainties 10% and 9 combinations of  $b=0.1/0.5/0.9$  and  $c=0.1/0.5/0.9$ .

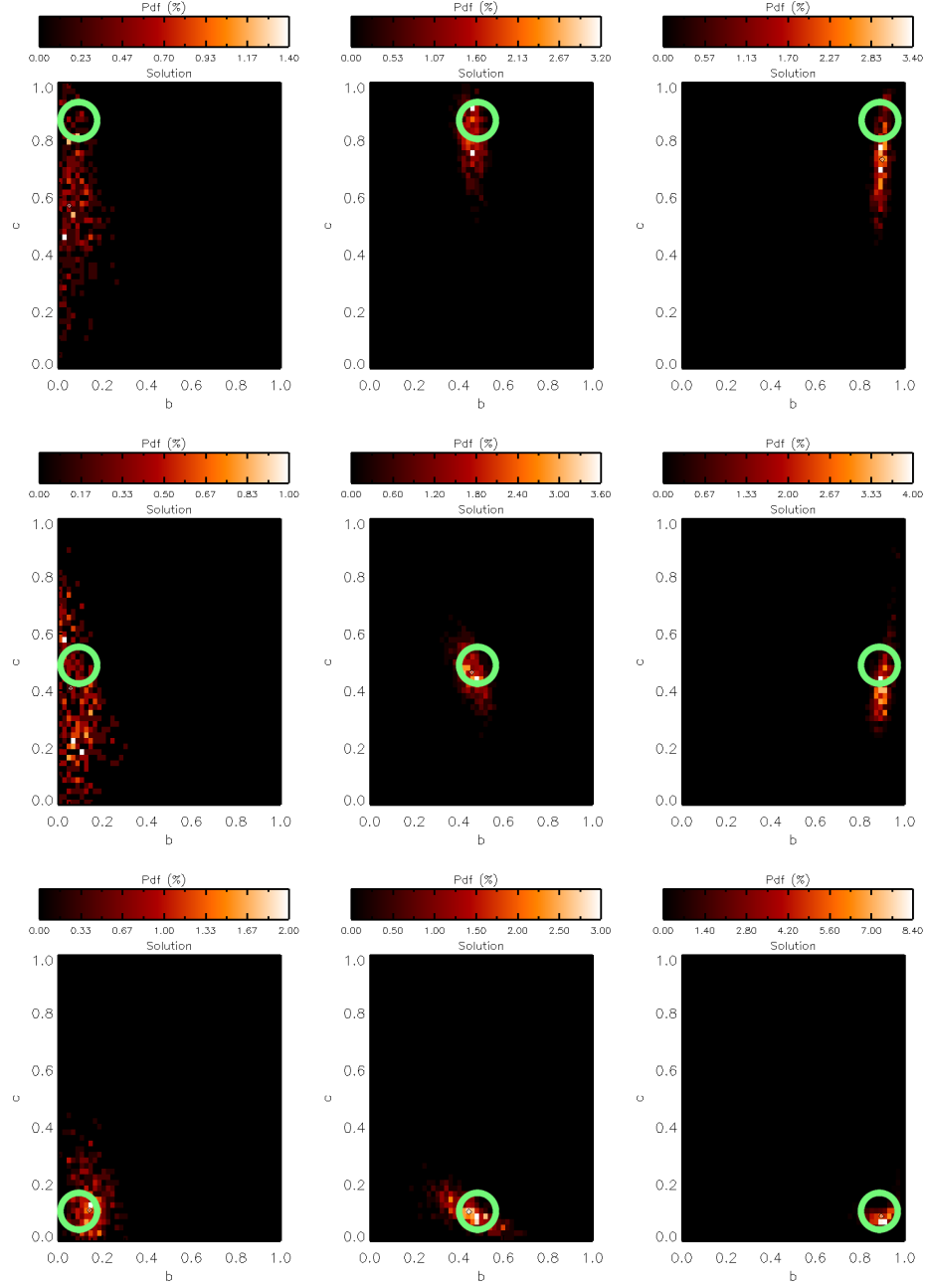


Figure 18: Same as fig. 17 but using the Fast Monte Carlo method explained in section 2.5.

- For data uncertainty less than 5%, the parameters can be estimated using single EPF under certain geometric configurations: close to the principal plane (azimuthal angle less than  $45^\circ$ ) and high incidence angles (greater than  $50^\circ$ ) leading to a broad phase angle range, containing low and high phase angles, to sufficiently describe the shape of the photometric curve.
- In the case of one single observation, with each pixel considered as a facet with known geometry,  $\omega$  can be retrieved with small uncertainties ( $1\sigma$  uncertainties  $\leq 0.1$ ), but also  $b$ ,  $c$  and in some extent  $\bar{\theta}$ , in the case of very extreme phase function. This case is equivalent to one disk resolved image of a planetary body, assumed to be homogeneous in surface properties.
- Full BRDF observations allowing a high diversity of geometric sampling are the best configurations to constrain all the parameter set:  $\omega$ ,  $b$ ,  $c$  and  $\bar{\theta}$ . This geometric conditions can be easily reproduced in laboratory and can be obtained by combining different EPF observations at varied illumination conditions and/or varied azimuthal planes. Nevertheless, even BRDF measurements are limited by the phase range. Our results indicate that a favorable EPF with higher phase range than a BRDF is better to constraint the parameters.
- A favorable EPF measurement (i.e., principal plane, incidence at  $75^\circ$ , emergence angle sampling up to  $80^\circ$ ) is better to constrain the parameters than a standard EPF (incidence at  $40^\circ$  and  $60^\circ$ , emergence up to  $70^\circ$ ), most probably due to better high phase angle sampling.
- The hockey stick relationship on the  $b$  vs  $c$  diagram may be the result of the non-linearity of the Hapke model if the data are from a EPF type observation and the inversion strategy is based on simple mean square minimization. However, the Full BRDF type observations are not biased by the non-linearity. Because the data used in the Hapke (2012) synthesis are generally BRDF type observations (Hapke, 2012), it is unlikely that the hockey stick relationship is an artifact from the inversion method. This confirms that surface material with strongly backward scattering with narrow lobe may not exist in the nature.

Future work should include real laboratory spectra and datasets on planetary bodies with prioritization using the conclusion of this study. Also the wavelength dependance of all parameters should be addressed. Finally, the latest developments of the Hapke model should be included within this inversion strategy in order to compare the actual properties of the granular material and retrieved photometric parameters, given precise uncertainties.

#### *Acknowledgement*

We acknowledge support from the “Institut National des Sciences de l’Univers” (INSU), the “Centre National de la Recherche Scientifique” (CNRS) and “Centre National d’Etude Spatiale” (CNES) and through the “Programme National de Planétologie” and MEX/OMEGA Program.

## References

- Baratoux, D., Pinet, P. C., Kaydash, V. G., Shkuratov, Y., Daydou, Y., Besse, S., Jehl, A., Chevrel, S., Mar. 2006. The Derivation of Hapke Parameters Using Multi-Angular Observations from Orbit and Laboratory: An Ill-posed Problem. In: Mackwell, S., Stansbery, E. (Eds.), 37th Annual Lunar and Planetary Science Conference. Vol. 37 of Lunar and Planetary Science Conference. p. 1340.
- Beck, P., Pommerol, A., Thomas, N., Schmitt, B., Moynier, F., Barrat, J.-A., Mar. 2012. Photometry of meteorites. *Icarus* 218 (1), 364–377.  
URL <http://www.sciencedirect.com/science/article/pii/S0019103511004702>
- Ceamanos, X., Douté, S., Fernando, J., Schmidt, F., Pinet, P., Lyapustin, A., Mar. 2013. Surface reflectance of Mars observed by CRISM/MRO: 1. Multi-angle Approach for Retrieval of Surface Reflectance from CRISM observations (MARS-ReCO). *Journal of Geophysical Research (Planets)* 118, 514–533.
- Chandrasekhar, S., 1960. Radiative transfer. New York: Dover, 1960.
- Cheng, A. F., Domingue, D. L., Apr. 2000. Radiative transfer models for light scattering from planetary surfaces. *Journal of Geophysical Research* 105, 9477–9482.
- Cord, A. M., Pinet, P. C., Daydou, Y., Chevrel, S. D., Oct. 2003. Planetary regolith surface analogs: optimized determination of hapke parameters using multi-angular spectro-imaging laboratory datas. *Icarus* 165 (2), 414–427.  
URL <http://www.sciencedirect.com/science/article/B6WGF-49CSWKN-4/2/ed4f0b878ce8f0cc56dd37d6cce6c772>
- Fernando, J., Schmidt, F., Ceamanos, X., Pinet, P., Douté, S., Daydou, Y., Mar. 2013. Surface reflectance of Mars observed by CRISM/MRO: 2. Estimation of surface photometric properties in Gusev Crater and Meridiani Planum. *Journal of Geophysical Research (Planets)* 118, 534–559.  
URL <http://arxiv.org/abs/1303.4549>
- Fernando, J., Schmidt, F., Pilorget, C., Pinet, P., Ceamanos, X., Douté, S., Daydou, Y., Costard, F., 2015. Characterization and mapping of surface physical properties of mars from {CRISM} multi-angular data: Application to gusev crater and meridiani planum. *Icarus* 253 (0), 271 – 295.  
URL <http://www.sciencedirect.com/science/article/pii/S0019103515001128>
- Fisher, R. A., Jan. 1930. Moments and product moments of sampling distributions. *Proceedings of the London Mathematical Society* s2-30 (1), 199–238.  
URL <http://plms.oxfordjournals.org/content/s2-30/1/199.short>



- Gunderson, K., Thomas, N., Whitby, J., 2006. First measurements with the physikalisches institut radiometric experiment (phire). Planetary and Space Science 54 (11), 1046 – 1056, simulations in Laboratory Experiments, Instrumentation and Modelling for Space Applications European Geosciences Union General Assembly - Session {PS} 9.  
URL <http://www.sciencedirect.com/science/article/pii/S003206330600105X>
- Haario, H., Saksman, E., Tamminen, J., 04 2001. An adaptive metropolis algorithm. Bernoulli 7 (2), 223–242.  
URL <http://projecteuclid.org/euclid.bj/1080222083>
- Hapke, B., 1981. Bidirectional reflectance spectroscopy 1. theory. J. Geophys. Res. 86, –.  
URL <http://dx.doi.org/10.1029/JB086iB04p03039>
- Hapke, B., Jul. 1984. Bidirectional reflectance spectroscopy. III - Correction for macroscopic roughness. Icarus 59, 41–59.
- Hapke, B., Aug. 1986. Bidirectional reflectance spectroscopy. IV - The extinction coefficient and the opposition effect. Icarus 67, 264–280.
- Hapke, B., 1993. Theory of reflectance and emittance spectroscopy. Topics in Remote Sensing, Cambridge, UK: Cambridge University Press.
- Hapke, B., Jun. 1996. Are planetary regolith particles back scattering? response to a paper by m. mishchenko. Journal of Quantitative Spectroscopy and Radiative Transfer 55 (6), 837–848.  
URL <http://www.sciencedirect.com/science/article/pii/S0022407395001905>
- Hapke, B., Jun. 2002. Bidirectional Reflectance Spectroscopy5. The Coherent Backscatter Opposition Effect and Anisotropic Scattering. Icarus 157, 523–534.
- Hapke, B., Jun. 2008. Bidirectional reflectance spectroscopy: 6. effects of porosity. Icarus 195 (2), 918–926.  
URL <http://www.sciencedirect.com/science/article/B6WGF-4RR8YWH-2/1/a50020f57fb3b60836f4511a299f1e1a>
- Hapke, B., Nov. 2012. Bidirectional reflectance spectroscopy 7: The single particle phase function hockey stick relation. Icarus 221 (2), 1079–1083.  
URL <http://www.sciencedirect.com/science/article/pii/S0019103512004319>
- Hapke, B., Feb. 2013. Comment on "a critical assessment of the hapke photometric model" by y. shkumatov et al. Journal of Quantitative Spectroscopy and Radiative Transfer 116 (0), 184–190.  
URL <http://www.sciencedirect.com/science/article/pii/S0022407312004888>

- Hapke, B., R. Nelson, R., Smythe, W., 1998. The opposition effect of the moon: coherent backscatter and shadow hiding. *Icarus* 133, 89–97.
- Hapke, B., Wells, E., 1981. Bidirectional reflectance spectroscopy 2. experiments and observations. *J. Geophys. Res.* 86, –.  
URL <http://dx.doi.org/10.1029/JB086iB04p03055>
- Helfenstein, P., Veverka, J., 1989. Physical characterization of asteroid surfaces from photometric analysis. In: Binzel, R. P., Gehrels, T., Matthews, M. S. (Eds.), *Asteroids II*. pp. 557–593.
- Heney, L. G., Greenstein, J. L., Jan. 1941. Diffuse radiation in the Galaxy. *Astrophysical Journal* 93, 70–83.
- Jehl, A., Pinet, P., Baratoux, D., Daydou, Y., Chevrel, S., Heuripeau, F., Manaud, N., Cord, A., Rosenberg, C., Neukum, G., Gwinner, K., Scholten, F., Hoffman, H., Roatsch, T., Oct. 2008. Gusev photometric variability as seen from orbit by hrsc/mars-express. *Icarus* 197 (2), 403–428.  
URL <http://www.sciencedirect.com/science/article/B6WGF-4STB0J6-3/2/7d905531eed585267c03cc94b4a3e60f>
- Johnson, J. R., Grundy, W. M., Lemmon, M. T., Bell, J. F., Johnson, M. J., Deen, R., Arvidson, R. E., Farrand, W. H., Guinness, E., Hayes, A. G., Herkenhoff, K. E., Seelos, F., Soderblom, J., Squyres, S., Dec. 2006a. Spectrophotometric properties of materials observed by pancam on the mars exploration rovers: 2. opportunity. *J. Geophys. Res.* 111 (E12), E12S16–.  
URL <http://dx.doi.org/10.1029/2006JE002762>
- Johnson, J. R., Grundy, W. M., Lemmon, M. T., Bell, J. F., Johnson, M. J., Deen, R. G., Arvidson, R. E., Farrand, W. H., Guinness, E. A., Hayes, A. G., Herkenhoff, K. E., Seelos, F., Soderblom, J., Squyres, S., Feb. 2006b. Spectrophotometric properties of materials observed by pancam on the mars exploration rovers: 1. spirit. *J. Geophys. Res.* 111 (E2), E02S14–.  
URL <http://dx.doi.org/10.1029/2005JE002494>
- Johnson, J. R., Kirk, R., Soderblom, L. A., Gaddis, L., Reid, R. J., Britt, D. T., Smith, P., Lemmon, M., Thomas, N., Bell, J. F., Bridges, N. T., Anderson, R., Herkenhoff, K. E., Maki, J., Murchie, S., Dummel, A., Jaumann, R., Trauthan, F., Arnold, G., Apr. 1999. Preliminary results on photometric properties of materials at the sagan memorial station, mars. *J. Geophys. Res.* 104 (E4), 8809–8830.  
URL <http://dx.doi.org/10.1029/98JE02247>
- Johnson, J. R., Shepard, M. K., Grundy, W. M., Paige, D. A., Foote, E. J., Mar. 2013. Spectrogoniometry and modeling of martian and lunar analog samples and apollo soils. *Icarus* 223 (1), 383–406.  
URL <http://www.sciencedirect.com/science/article/pii/S0019103512004988>

- Mishchenko, M. I., Jul. 1994. Asymmetry parameters of the phase function for densely packed scattering grains. *Journal of Quantitative Spectroscopy and Radiative Transfer* 52 (1), 95–110.  
URL <http://www.sciencedirect.com/science/article/pii/S0022407394901422>
- Mosegaard, K., Tarantola, A., Jul. 1995. Monte Carlo sampling of solutions to inverse problems. *Journal of Geophysical Research* 100, 12431–12448.
- Murchie, S., Arvidson, R., Bedini, P., Beisser, K., Bibring, J.-P., Bishop, J., Boldt, J., Cavender, P., Choo, T., Clancy, R. T., Darlington, E. H., Des Marais, D., Espiritu, R., Fort, D., Green, R., Guinness, E., Hayes, J., Hash, C., Heffernan, K., Hemmler, J., Heyler, G., Humm, D., Hutcheson, J., Izenberg, N., Lee, R., Lees, J., Lohr, D., Malaret, E., Martin, T., McGovern, J. A., McGuire, P., Morris, R., Mustard, J., Pelkey, S., Rhodes, E., Robinson, M., Roush, T., Schaefer, E., Seagrave, G., Seelos, F., Silverglate, P., Slavney, S., Smith, M., Shyong, W.-J., Strohhahn, K., Taylor, H., Thompson, P., Tossman, B., Wirzbarger, M., Wolff, M., May 2007. Compact reconnaissance imaging spectrometer for mars (crism) on mars reconnaissance orbiter (mro). *J. Geophys. Res.* 112 (E5), E05S03–.  
URL <http://dx.doi.org/10.1029/2006JE002682>
- Mustard, J. F., Pieters, C. M., 1989. Photometric phase functions of common geologic minerals and applications to quantitative analysis of mineral mixture reflectance spectra. *J. Geophys. Res.* 94, –.  
URL <http://dx.doi.org/10.1029/JB094iB10p13619>
- Pommerol, A., Thomas, N., Jost, B., Beck, P., Okubo, C., McEwen, A. S., Oct. 2013. Photometric properties of mars soils analogs. *J. Geophys. Res. Planets* 118, 1–28.  
URL <http://dx.doi.org/10.1002/jgre.20158>
- Sato, H., Robinson, M. S., Hapke, B., Denevi, B. W., Boyd, A. K., 2014. Resolved hapke parameter maps of the moon. *Journal of Geophysical Research: Planets* 119, 1775–1805.  
URL <http://dx.doi.org/10.1002/2013JE004580>
- Shepard, M. K., Helfenstein, P., 2007. A test of the hapke photometric model. *Journal of Geophysical Research: Planets* 112 (E3), n/a–n/a.  
URL <http://dx.doi.org/10.1029/2005JE002625>
- Shkuratov, Y., Kaydash, V., Korokhin, V., Velikodsky, Y., Petrov, D., Zubko, E., Stankevich, D., Videen, G., Dec. 2012. A critical assessment of the hapke photometric model. *Journal of Quantitative Spectroscopy and Radiative Transfer* 113 (18), 2431–2456.  
URL <http://www.sciencedirect.com/science/article/pii/S0022407312001926>

- Souchon, A., Pinet, P., Chevrel, S., Daydou, Y., Baratoux, D., Kurita, K., Shepard, M., Helfenstein, P., Sep. 2011. An experimental study of hapke's modeling of natural granular surface samples. *Icarus* 215 (1), 313–331.  
 URL <http://www.sciencedirect.com/science/article/pii/S0019103511002405>
- Tarantola, A., Valette, B., 1982. Inverse Problems = Quest for Information. *Journal of Geophysics* 50, 159–170.
- Vincendon, M., 2013. Mars surface phase function constrained by orbital observations. *Planetary and Space Science* 76 (0), 87 – 95.  
 URL <http://www.sciencedirect.com/science/article/pii/S0032063312003820>
- Yokota, Y., Matsunaga, T., Ohtake, M., Haruyama, J., Nakamura, R., Yamamoto, S., Ogawa, Y., Morota, T., Honda, C., Saiki, K., Nagasawa, K., Kitazato, K., Sasaki, S., Iwasaki, A., Demura, H., Hirata, N., Hiroi, T., Honda, R., Iijima, Y., Mizutani, H., Oct. 2011. Lunar photometric properties at wavelengths 0.5-1.6  $\mu$ m acquired by selene spectral profiler and their dependency on local albedo and latitudinal zones. *Icarus* 215 (2), 639–660.  
 URL <http://www.sciencedirect.com/science/article/pii/S0019103511003009>